Chapter 6: Strengthening and ductilization of low-density duplex steel by electropulsing treatment

6.1 Introduction

The present investigation finds the effect of electropulsing treatment on the mechanisms of refining and reprecipitation of ordered $L2_0$ structure (B2) in annealed (PD3-A) and aged (PD3-AB_{30}) duplex low density steel of Fe-18Mn-10.5Al-1C-6Ni composition. The Chapter also describes the impact of microstructural changes (due to electropulsing) on tensile properties.

6.2 Effect of electropulsing on PD3-A

6.2.1 Results

The microstructure of PD3-A steel depicts the presence of the banded B2 phase with an average width of 8.2 ± 2.7 μm and length of 18.1 ± 5.1 μm (Figure 6.1 (a)), B2 platelets with a width of 0.21 ± 0.08 μm, and the length of 0.79 ± 0.25 μm (Figure 6.1 (c), (e)), and globular B2 structure of average diameter of 1.40 ± 0.6 μm (Figure 6.1 (c)) are observed within the austenitic matrix. B2 is an order phase of $L2_0$ structure. Energy dispersive spectroscopic study has been performed on all three types of B2, i.e. banded, globular and platelet. The constituent elements in banded B2 are 11.58 % Mn-16.74% Al-15.55% Ni and balance Fe, respectively. On the other hand, the globular B2 has compositions of 13.87% Mn-15.41% Al-12.55% Ni and balance Fe. The measured composition of B2 platelet is 17.24% Mn-10.90% Al-5.86% Ni and balance Fe. After electropulsing treatment of PD3-A, in PD3-AE, B2 precipitate morphologies are refined. The width of banded,

platelet B2 reduces to 5.5 ± 2.0 μm and 0.14 ± 0.04 μm (Figure 6.1 (b), (d)) respectively. On the other hand, the length of bands and platelets are also reduced to 14.5 ± 7.3 μm, and

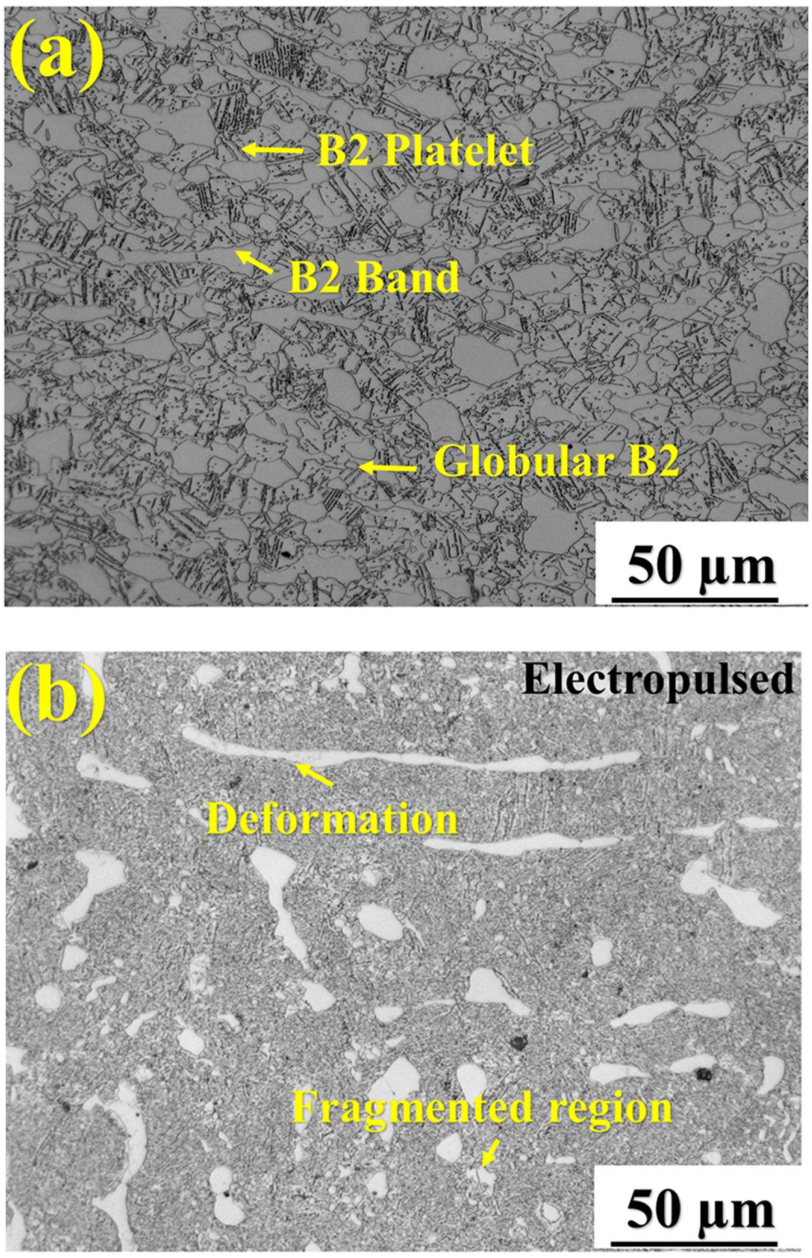

Figure 6.1: (a) Optical micrograph, (c) secondary electron micrograph, and (e) magnified secondary electron micrograph of PD3-A sample depicting B2 platelets, globular B2 and banded B2 structures (as indicated by yellow arrows) in austenite matrix, (b) optical micrograph displaying deformed and fragmented B2 (d) secondary electron micrograph, and (f) magnified secondary electron micrograph of PD3-AE sample showing disintegrated, spheroidized B2 and B2 precipitate.

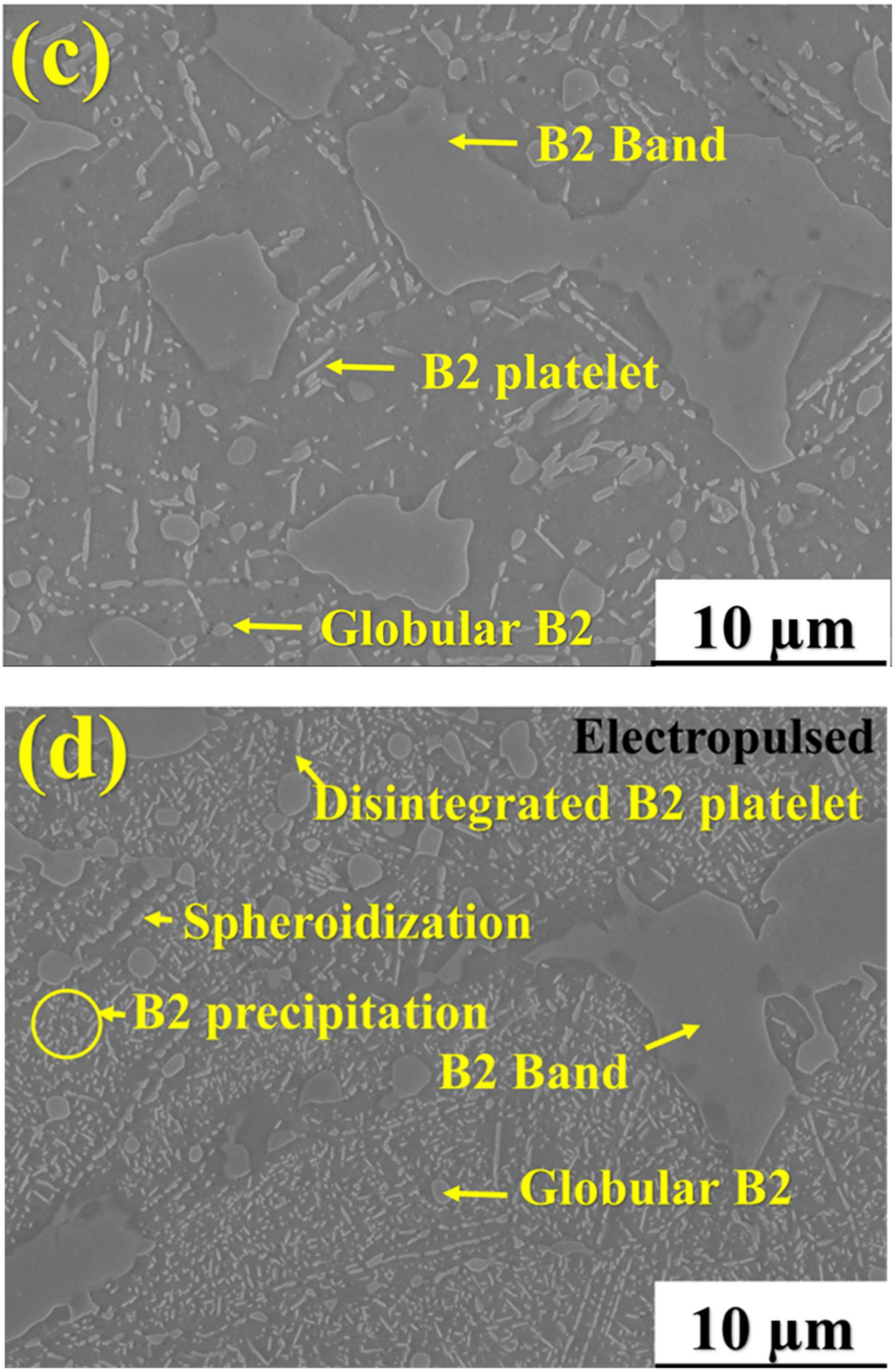

Figure 6.1. Continued.

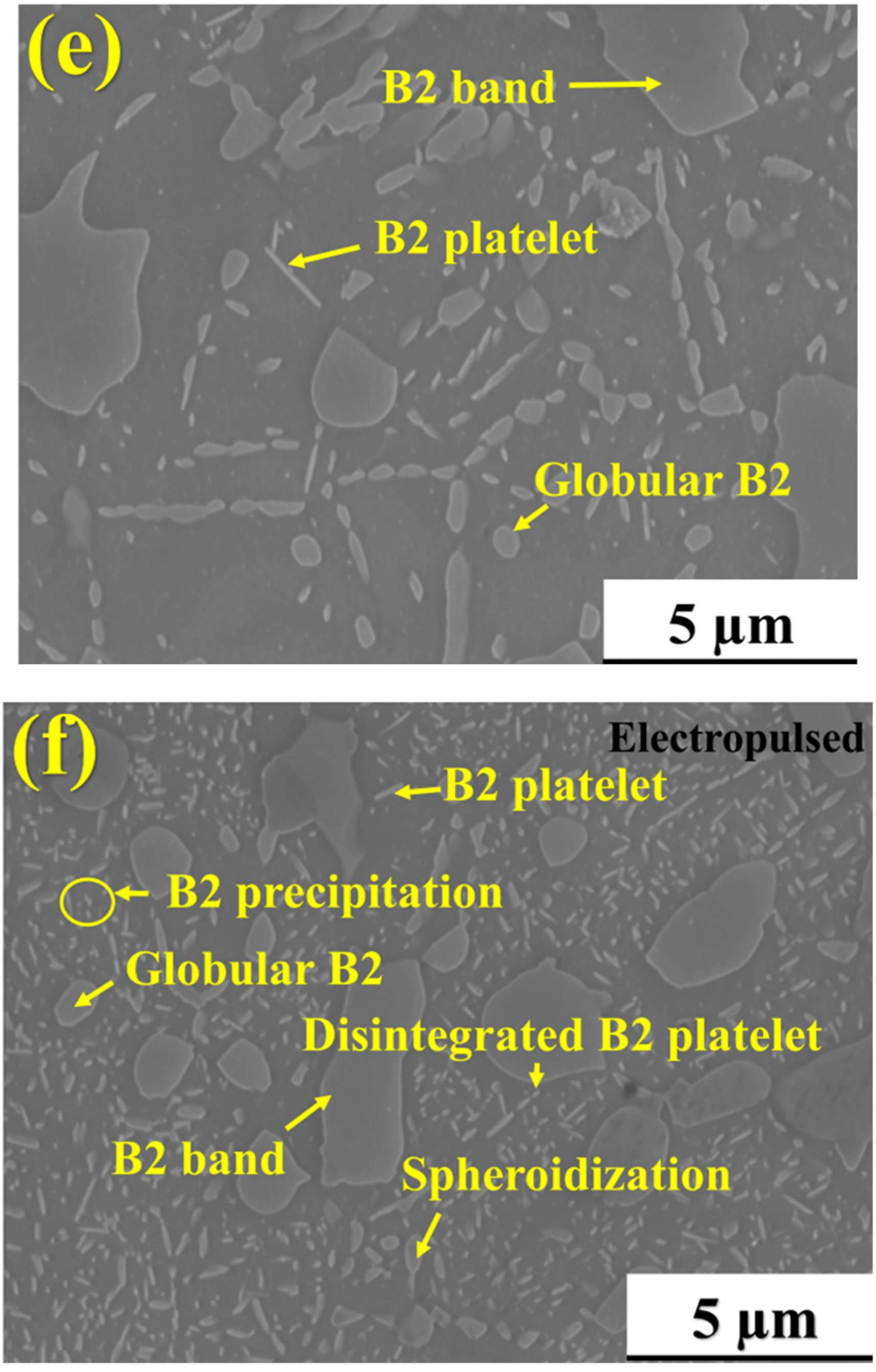

Figure 6.1. Continued.

0.59 ± 0.15 µm (Figure 6.1 (b), (f)). The diameter of globular B2 is also decreased to 0.85 ± 0.31 µm (Figure 6.1 (f)). Analysis of XRD patterns confirms the presence of austenite and B2 phases with volume percentages of 82%, and 18%, respectively in the PD3-A sample (Figure 6.2) and 77%, 23%, respectively in PD3-AE one (Figure 6.2). The dislocation densities in austenite and B2 (Figure 6.2), are calculated to be 2.9 x $10^{14}/m^2$, 5.4 x $10^{14}/m^2$ respectively. They are reduced to corresponding values of 0.20 x $10^{14}/m^2$, 2.31 x $10^{14}/m^2$ after electropulsing in PD3-AE (Figure 6.2). No precipitation of kappa carbide is observed in PD3-A (as per XRD and TEM) or PD3-AE samples (as per XRD pattern). Austenite has a face-centered cubic structure of lattice parameter of 3.60 Å.

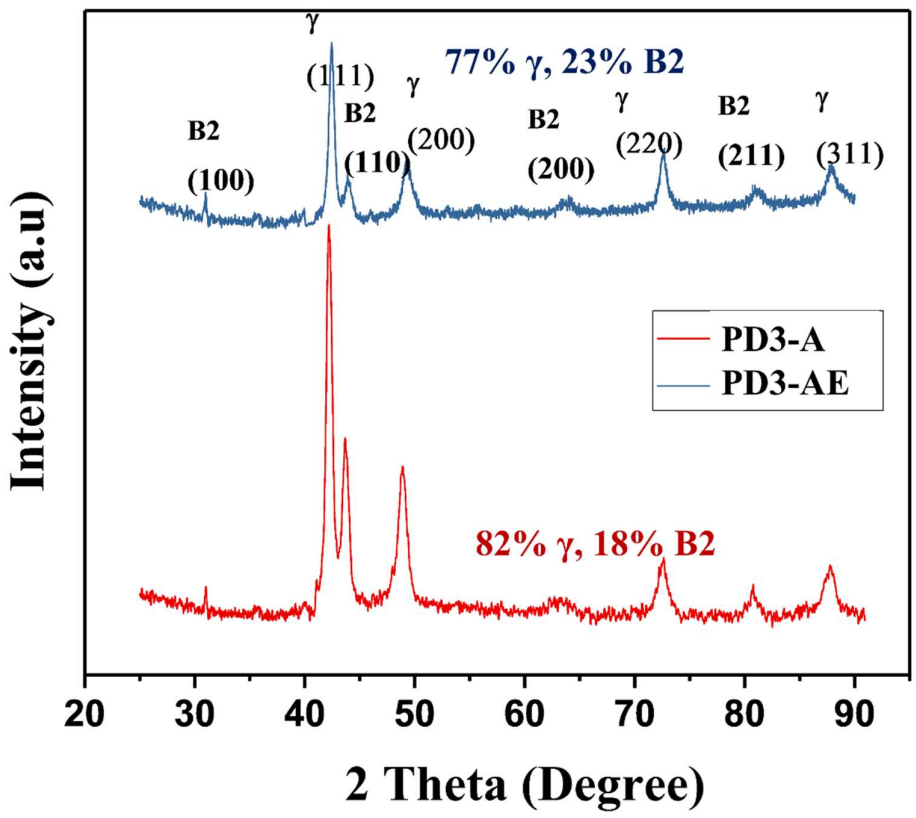

Figure 6.2: XRD patterns of PD3-A sample and PD3-AE samples conforming the presence of austenite and ordered B2 phases.

The image quality maps of the B2 phase and austenite with superimposed grain boundaries for PD3-A and PD3-AE samples shows that under electropulsing, dislocations are rearranged (Figures. 6.3 (a)-(d)). As a result, the low angle boundary (LAGB) fraction in B2 increases sharply from 40.4 % to 86.7% (Figure 6.3 (a)-(b)) and the average high angle grain boundary (HAGB) fraction decreases significantly from 59.6% to 13.3%. On electropulsing, in PD3-AE, the average Misorientation angle (MA) of B2 has decreased marginally (Figure 6.3 (e)). In the annealed sample (PD3-A), the distribution of low-angle or high-angle boundaries of austenite is almost uniform (Figure 6.3(c)). After electropulsing, in PD3-AE even though the overall LAGB or HAGB fraction of austenite remains almost constant, the localized fractions are much different (located by two encircled areas A1, A2 in Figure 6.3 (d)). In areas away from the coarse-size banded B2, the matrix austenite (A1) is recovered, and the LAGB fraction records a very high value. On the other hand, in areas near banded B2, the HAGB fraction is significantly enhanced (A2), i.e. austenite is recrystallized. Number fraction vs. misorientation angle (MA) of B2 and austenite for PD3-A and PD3-AE samples displays that there is an overall increase in the average MA of austenite from 12.8° to 16° (Figures. 6.4 (a)-(b)) as well as a reduction in KAM value (Figure 6.5 (a)-(b), Table 6.1). As shown in Table 1, In PD3-A, the B2 phase exhibits an average MOA of 25.53°, while in PD3-AE samples, it is 23.66°. For the austenite phase in PD3-A, the average MOA is 12.85°, while in PD3-AE samples, it increases to 16.05°. The decrease in MA suggests that more LAGB forms in the B2 phase, indicating deformation in the B2 phase. Conversely, the increase in the case of austenite suggests the coalescence of LAGB under electropulsing treatment. The marginal decrease in the KAM value suggests that electropulsing treatment reduces the dislocation density.

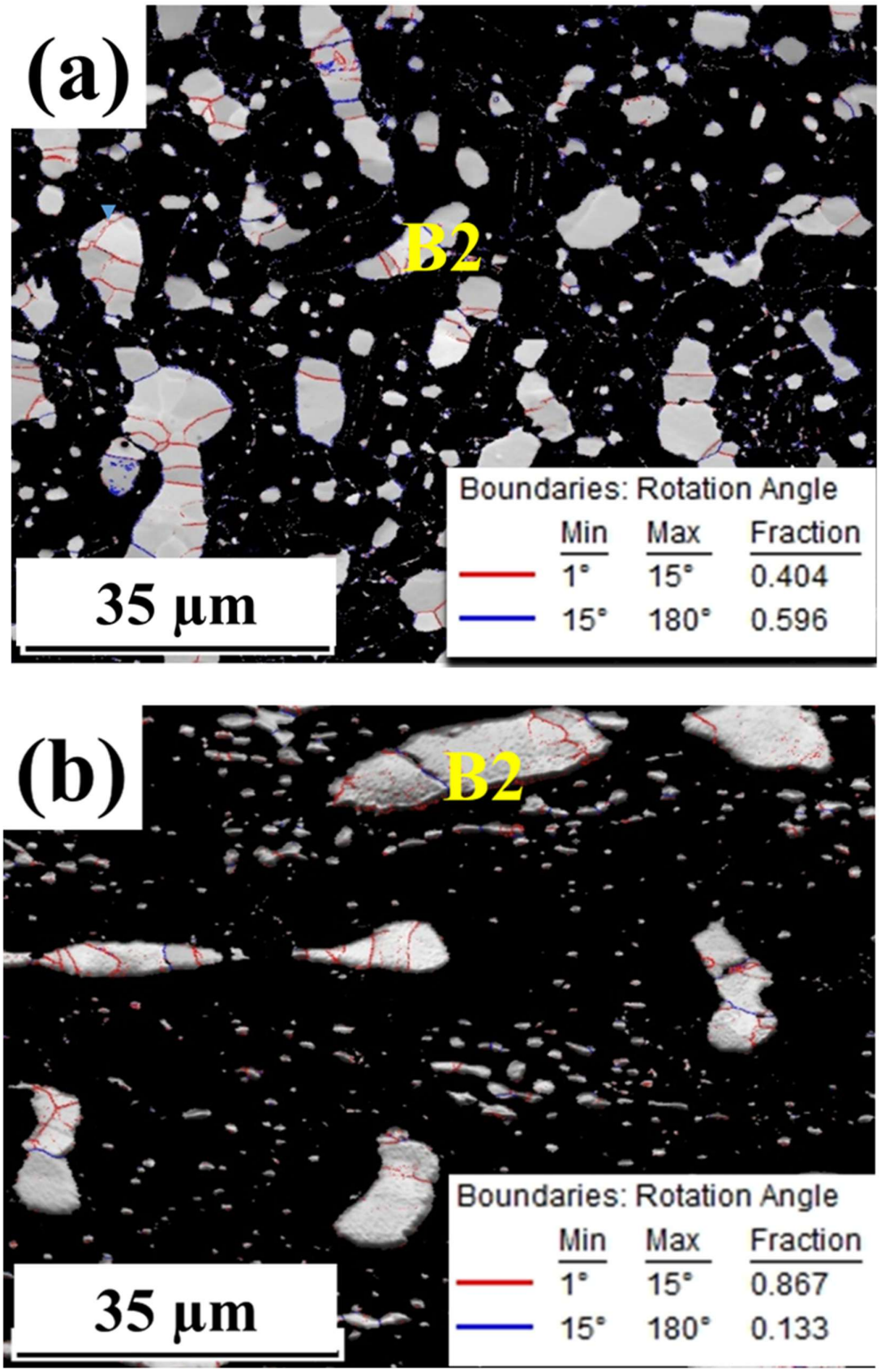

Figure 6.3: Image quality map with superimposed grain boundaries of (a) B2 (c) austenite in PD3-A sample, partially recovered austenite is encircled by yellow line, (b) B2 (d) austenite in PD3-AE sample.

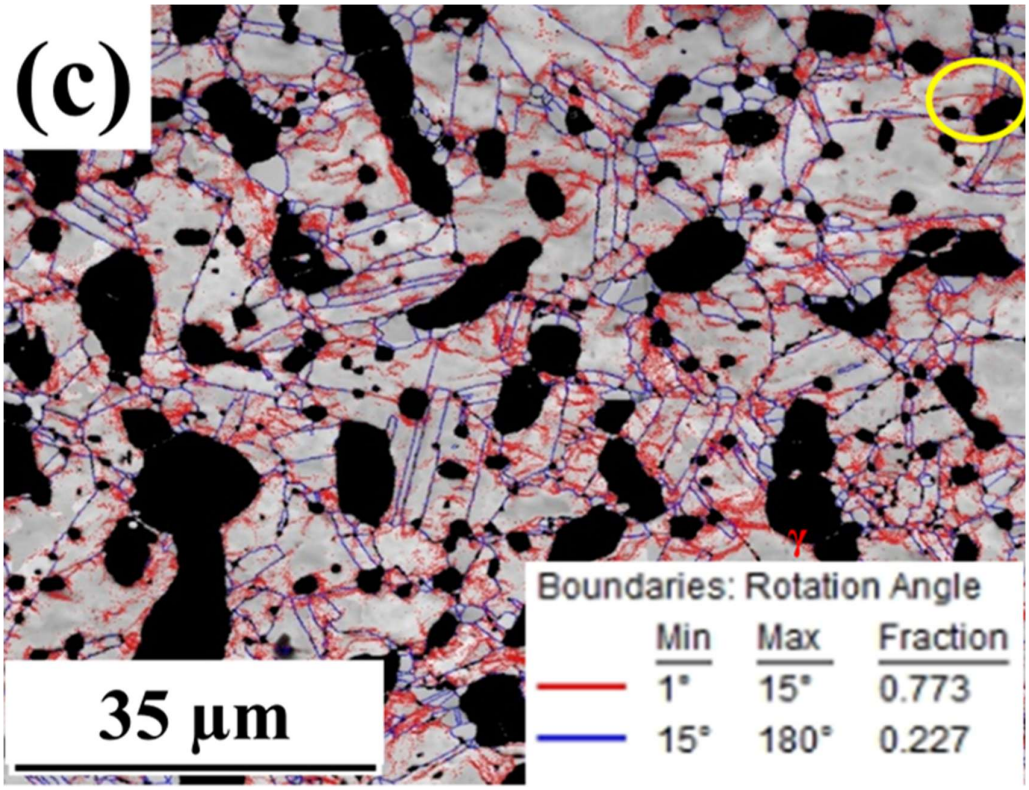

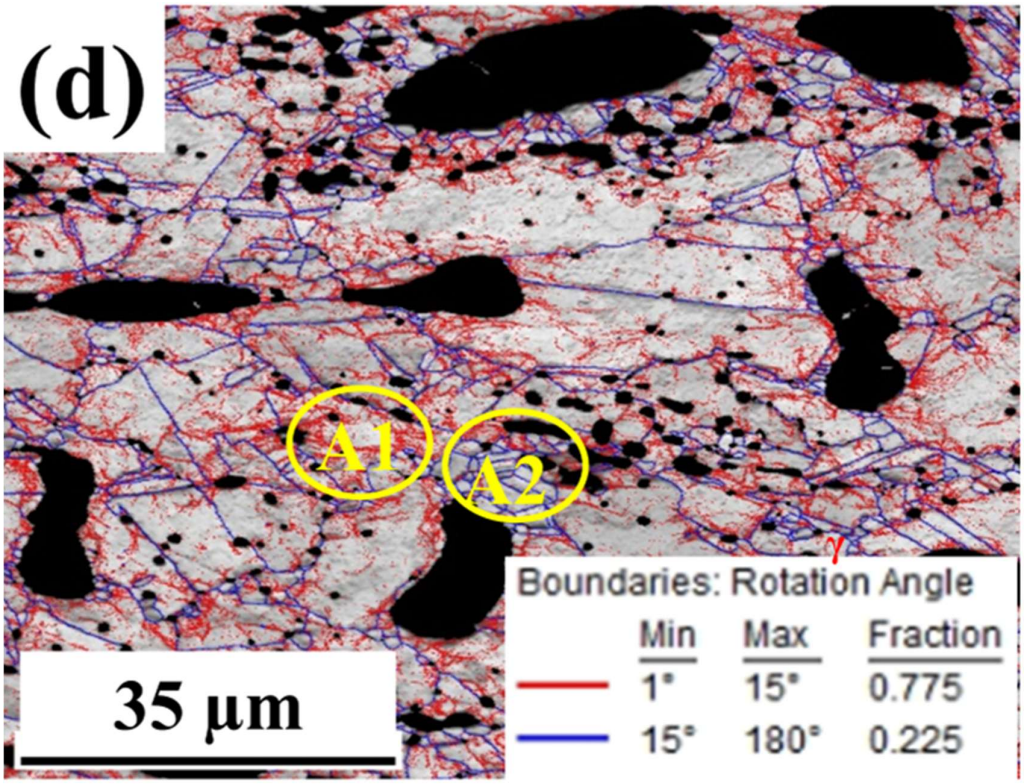

Figure 6.3. Continued.

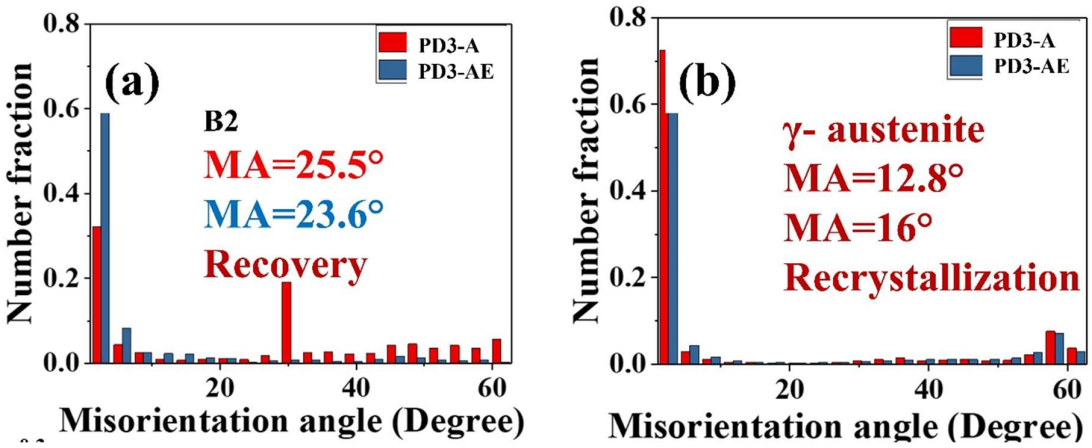

Figure 6.4: Number fraction vs misorientation angle of (a) B2 and (b) austenite in both PD3-A and PD3-AE samples. B2 is partly recovered, austenite is partially recrystallized.

Table 6.1: LAGB and HAGB fractions, average MA and KAM values of B2 and austenite.

Comparison	PD3-A		PD3-AE	
Phase	B2	Austenite	B2	Austenite
LAGB fraction	0.404	0.773	0.867	0.775
HAGB fraction	0.596	0.227	0.133	0.225
MA, (°)	25.5	12.85	23.6	16.0
KAM, (°)	0.36	0.60	0.35	0.56

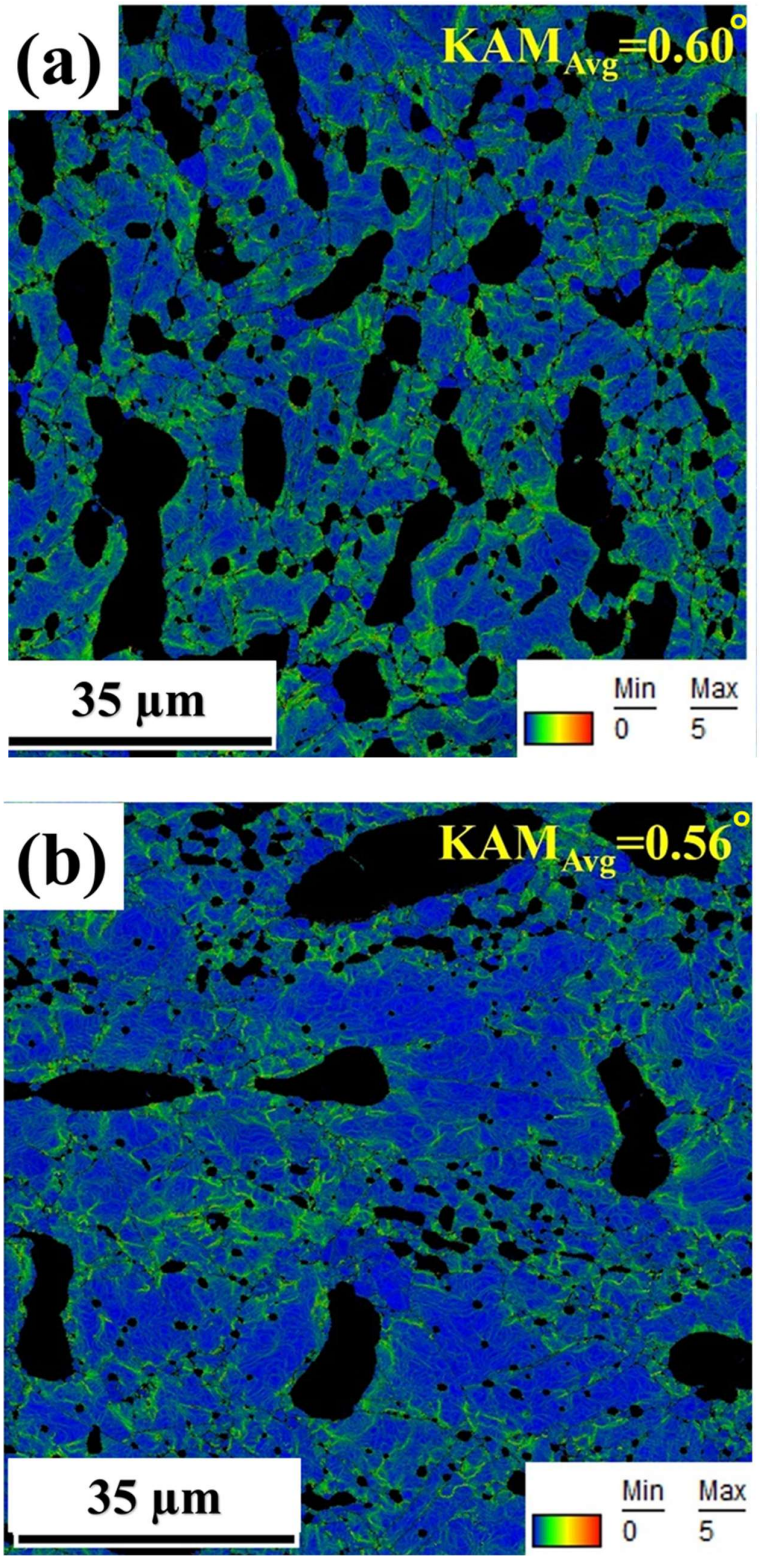

Figure 6.5: Kernel average misorientation maps of austenite in (a) PD3-A with average KAM value of 0.60° and (b) PD3-AE sample with average KAM value of 0.56° suggesting the strain is reduced by electropulsing treatment.

The orientation distribution function (ODF) representation of the texture of B2 phase in both samples exhibits rotated cube texture components (001) $[1\bar{1}0]$, (010) [101], (001) $[1\bar{1}0]$, (001) $[\bar{1}\bar{1}0]$ and (001) $[\bar{1}\bar{1}0]$ at positions of 1,2,3,4,5, with intensities of 15R, 14.9R,14.5R,14.4R, and 14.9R respectively in the PD3-A sample (Figure 6.6(a)) and 1, 2, 3, 4, 6 in the electropulsed sample with intensities of 14.3R (Figure 6.6(a)). At position 5 in the φ2 = 45˚ section, a component, (221) $[1\bar{1}0]$ as part of the alpha fiber is found with displaying rotated cube texture components at positions of 1, 2, 3, 4, 6 with reduced intensity and part of deformation texture alpha fiber at position 5, for austenite (Figure 6.6 (c)) PD3-A depicting Goss texture component at positions 1, 7, A component at positions 2, 5, a Goss twin-component at a position of 6, and S component at position 9 and (Figure 6.6 (d)) PD3-AE providing A component at positions 1 and 4 with decreased intensity and a new texture components at positions 2, 3, and 5 with the intensity of 8.3R in the electropulsed sample. In the PD3-A condition, the rotated component of B2 exhibits a maximum intensity of 15, which slightly reduces to 14.3 in the PD3-AE sample (Figure 6.6(b)). Austenite texture in the PD3-A sample mainly shows the Goss texture component with an intensity of 7.4R at positions 1, 7. A component with the intensity of 4.5R at positions 2, 5, a Goss twin-component with an intensity of 4.4R at a position of 6, and S component with the intensity of 3.1 R present in φ2 = 65 ˚ section at position 9 (Figure 6.6(c)). In the PD3-AE sample, the primary texture components are the A component, (110)$[1\bar{1}1]$, with an intensity of 5.5R at positions 1 and 4. Additionally, new texture components with an equal intensity of 6.4R are observed at positions 2, 3, and 5, characterized by Euler angles (ϕ_1, ϕ, ϕ_2) of (90,25,0), (90,65,0), and (0,90,65) with (hkl)<uvw> values of (012)$<0\bar{2}1>$, (021)$<0\bar{1}2>$, (210)$<1\bar{2}0>$ respectively (Figure 6.6(d)).

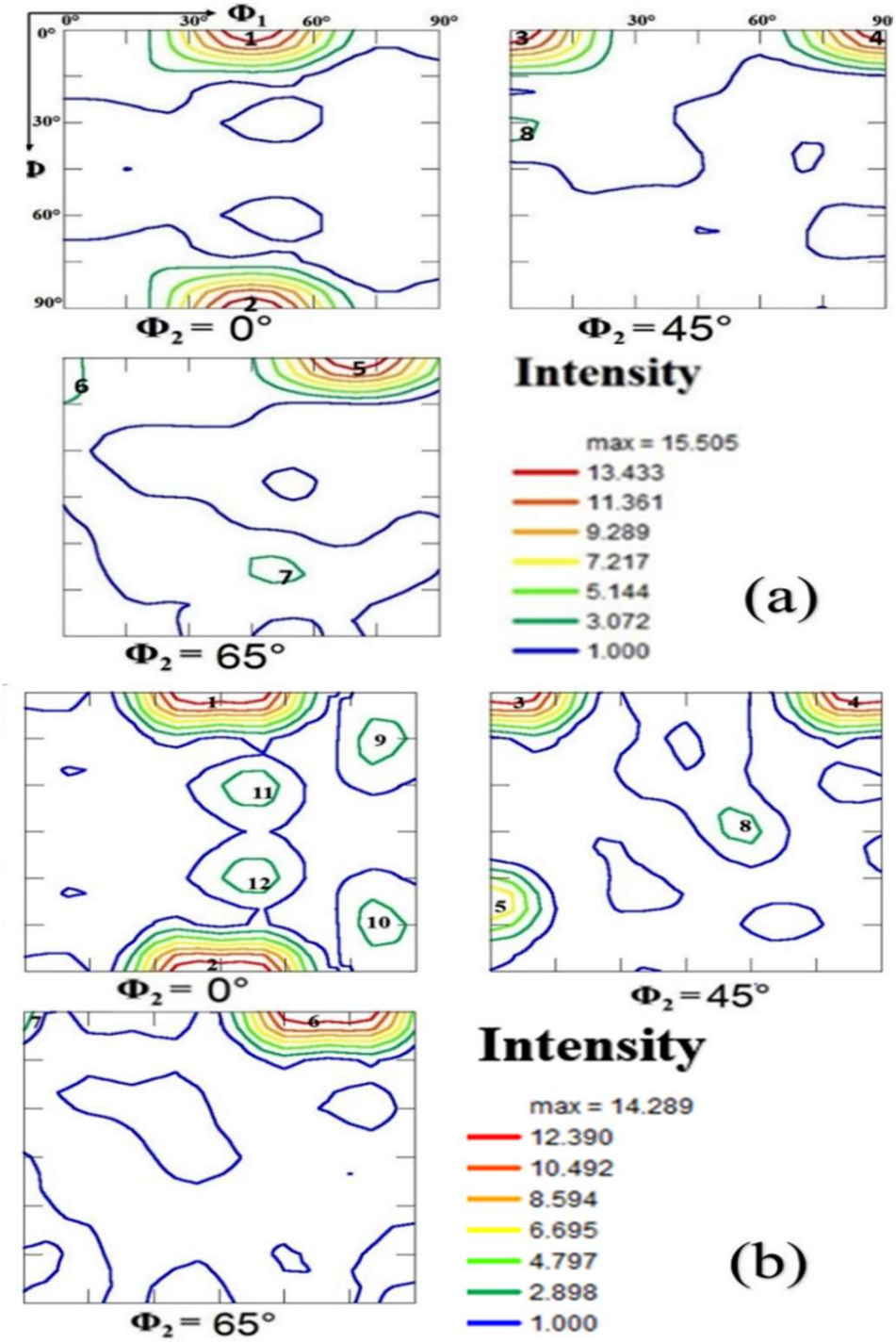

Figure 6.6: The orientation distribution function sections at φ2 =0°,45°, 65˚ for B2 (a) PD3-A showing rotated cube texture components at positions of 1,2,3,4,5, and (b) PD3-AE.

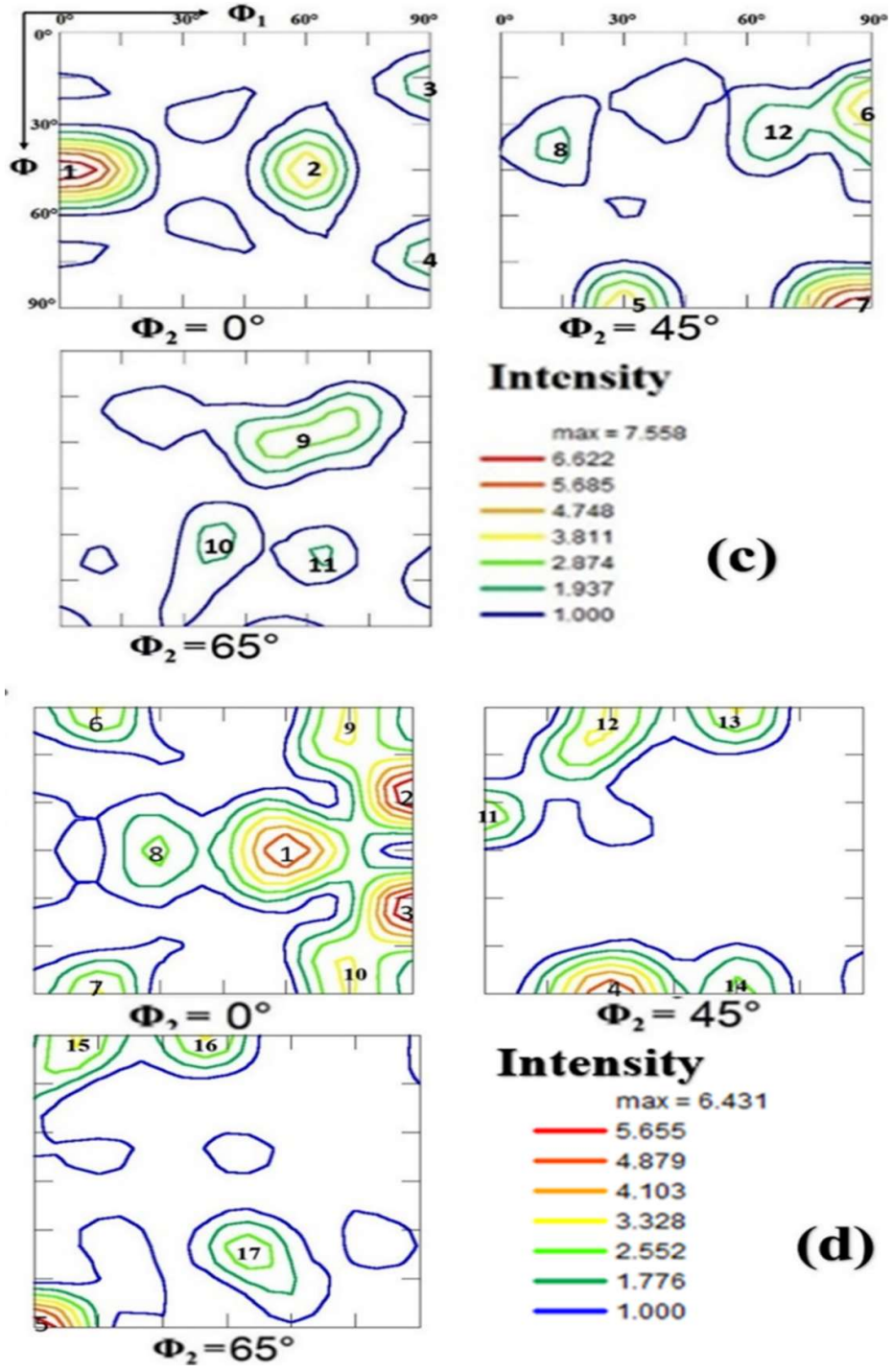

Figure 6.6. Continued.

The engineering stress-strain curve of PD3-A illustrates that annealed sample (PD3-A) reports a yield strength of 1015 ± 13 MPa ultimate tensile strength (UTS) of 1285 ± 17

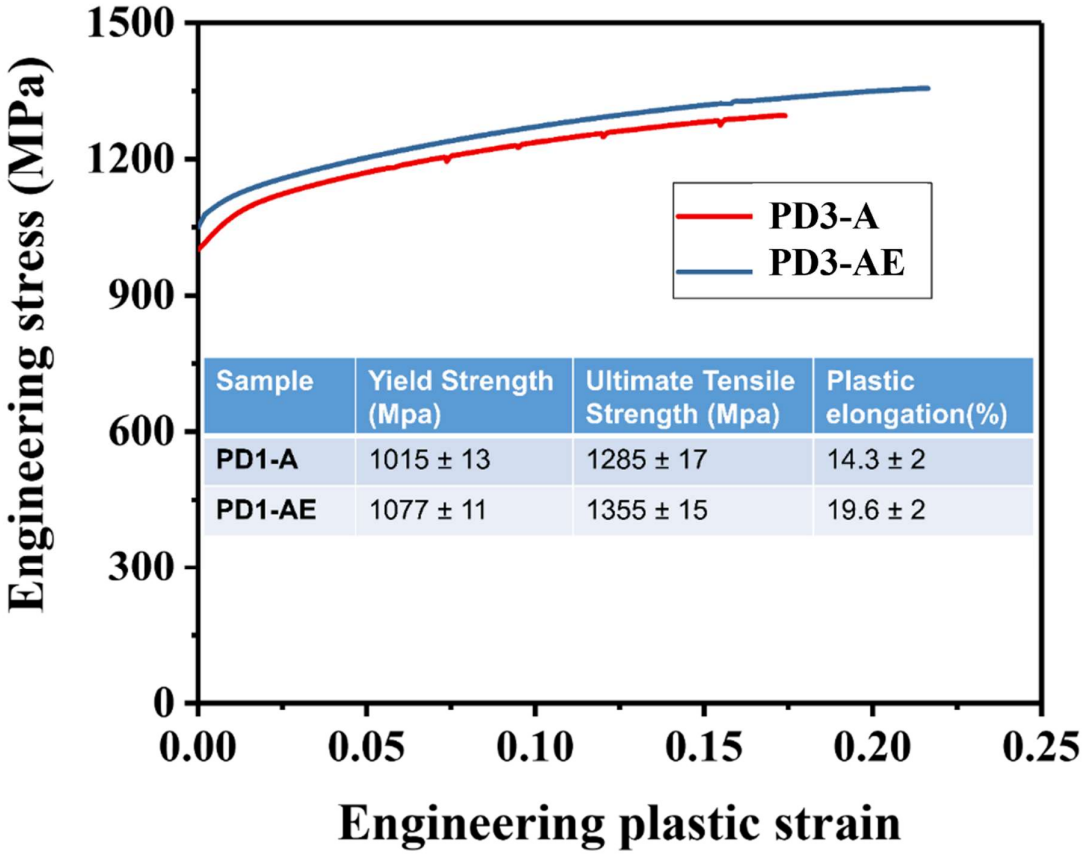

Sample	Yield Strength (Mpa)	Ultimate Tensile Strength (Mpa)	Plastic elongation(%)
PD1-A	1015 ± 13	1285 ± 17	14.3 ± 2
PD1-AE	1077 ± 11	1355 ± 15	19.6 ± 2

Figure 6.7: Engineering stress-plastic strain curves of annealed (PD3-A) and electropulsed (PD3-AE) low-density steels and the tensile properties are shown in table in the inset.

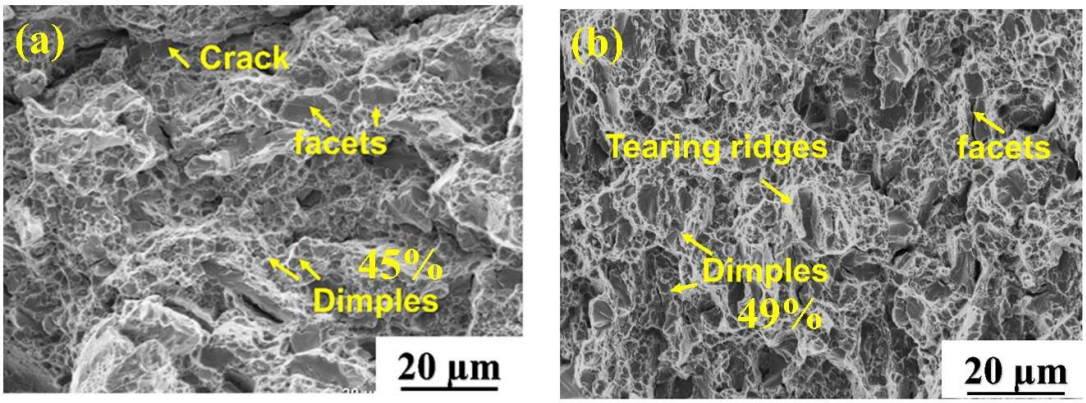

Figure 6.8: SEM fractographs of (a) Annealed (PD3-A) sample showing cracks, dimples and facets (b) electropulsed sample (PD3-AE) displays cracks of finer size, dimples of larger size and higher area fraction with reduced amount of facets.

MPa, and plastic elongation of 14.3 ± 2%. On electropulsing (PD3-AE), YS increases to 1077 ± 11 MPa, and UTS to 1355 ± 15 MPa, and interestingly the plastic elongation also increases to 19.6 ± 2%. Electropulsing enhances tensile strength as well as elongation.

The fractograph of the PD3-A sample and PD3-AE sample. An increase in the size of dimples with 1.736 ± 0.5 μm (Figure. 6.8 (b)) can be observed in the PD3-AE sample as compared to the PD3-A sample with a dimple size of 1.482 ± 0.4 μm (Figure. 6.8 (a)). The area percentage of dimples was also increased to 49.5% in comparison with that of the PD3-A sample which has 45%. Both samples displayed features resulting from mixed mode of ductile and brittle fracture.

6.2.2 Discussion

6.2.2.1 Microstructure

The optical and SEM micrographs provide distinct signatures of partial dissolution of B2 (all morphologies), its refinement, spheroidization, and precipitation of the B2 ordered phase by the electropulsing treatment of duplex low-density steel. Additionally, X-ray diffraction patterns provide evidence of reduced dislocation density, as calculated using the Williamson-Hall method. The observed microstructural modification by electropulsing treatment might have resulted from two possible mechanisms: thermal effects induced by Joule heating and athermal effects associated with electron wind force or atom diffusion.

6.2.2.2 Skin Depth Effect

During high-frequency electropulsing, the current is localized at the surface, a phenomenon known as the skin depth effect [148]. To assess the uniformity of current flow, the skin depth effect is estimated. The skin depth (δ) is calculated through the Equation 6.1 [149]:

$$\delta = \sqrt{\frac{\rho_r}{\pi F \mu_0 \mu_r}} \qquad [6.1]$$

Where F is the frequency of the pulse, μ_0 is the permeability in vacuum, and μ_r is the relative permeability, ρ_r is the resistivity of the sample. Taking F as 10.2 kHz in the present case, μ_0 as $4\pi*10^{-7}$ H/m, μ_r as 10 H/m [149], and measured ρ_r as $2.78*10^{-7}$ Ωm, skin depth (δ) is calculated to be 1.47 mm. The total skin depth is 2.94 mm which is much higher than the selected sample thickness of 2 mm. Therefore, the skin depth effect is not taken into consideration.

6.2.2.3 Thermal effect

The temperature rise due to Joule heating by an electropulse in the material can be estimated by Equation 6.2 as follows [150]:

$$\Delta T = \frac{\rho_r I^2 t_p}{d\, C_p} \qquad [6.2]$$

Where t_p is the time duration, C_p is the heat capacity, and d is the density of the sample. Substituting the values of I = $(7.5*10^9)$ A/m^2, tp = $(49*10^{-6})$ sec, ρ_r = $(2.787*10^{-7})$ Ω.m, d = $(6.67 * 10^3)$ Kg/m^3 and heat capacity as approximately 550 Jkg^{-1}K^{-1} [151]) into the equation, the temperature change due to Joule heating is calculated to be 209 K for the first cycle and the maximum temperature (T_{max}) rise is ($\Delta T + T_R$) 502K, where T_R is room temperature. When considering the initial peak current density and its corresponding pulse duration, the calculated temperature is only 228°C. This is a very low value compared to the theoretically expected precipitation formation temperature. While the measured temperature is 572 K, is also very low. Taking t_p as the total damping time of 283 μs and I_{av} as the average current density of $3.90*10^9$ A/m^2 the temperature of the sample is calculated to be 619 K(346°C). In summary, taking into account the overall duration of the damping wave and the mean current density, the calculated temperature of the pulsed sample is 346°C. The contribution from the entire pulse is obtained by taking I as average current density (determined by total area of pulse divided by total pulse time and cross-sectional area) and t_p as the total time duration of the entire pulse. The temperature

(temperature rise, ΔT + room temperature, 300K) of the sample due to entire pulse is calculated to be 346 °C. The actual temperature of the pulsed sample was measured by an infrared thermometer, to be 299°C. Literature shows precipitation temperature of the B2 phase is above 800 °C [75], [81]. Therefore, both the measured and analytical temperatures indicate that temperature effects can be taken as negligible.

6.2.2.4 Athermal effect

6.2.2.4.1 Dissolution of B2

Sizes of banded, globular, and platelets of B2 (Figure 6.1(b), (d), (f)) get reduced after electropulsing treatment due to dissolution. Athermal effect in the form of electron wind force is identified as the primary factor contributing to the resultant microstructure. Thermodynamic calculations by Dolinsky and Elperin elegantly support the concept that electropulsing tends to reconfigure the structure of material towards a state conducive to increased electrical conductivity. The reduction in the measured value of electrical resistivity of low-density steel from $2.78*10^{-7}$ Ωm before electopulsing to $1.63*10^{-7}$ Ωm after the treatment supports the concept of Dolinsky.

In physical terms, Bohenkamp's demonstration indicates that the inclusion of nickel in ferrite leads to an increase in its resistivity [152]. As per Matthiessen's theory [153] also, if the impurity concentration of the material is higher, the electrical resistivity of the material gets enhanced. In the present case, the content of Al is reduced from 16.74 to 9.52 %, and Ni from 15.55% to 14.5%, in B2 after electropulsing. This indicates a reduction in resistivity in the B2 phase by electropulsing. On the other hand, the electrical resistance also decreases with reduced length ($R = \rho * l/A$). Electropulsing, which aims to enhance conductivity or reduce resistance, decreases the size of the precipitate by partially dissolving it.

If transformation has to take place at a temperature (T) lower than the equilibrium temperature (T_e):

For dissolution of B2 in γ i.e. transformation of γ + B2 to γ', the total free energy change (ΔG_{EPT}) is the summation of barrier chemical energy change (ΔG_{Chem}), barrier interfacial energy (ΔG_{Inter}), and barrier strain energy (ΔG_{Strain}).

Under electropulsing conditions, an additional term (due to electropulsing), the change in free energy due to electric current (ΔG_{Elec}) can be included in the total free energy change (ΔG_{EPT}) which is given by Equation 6.3 [154].

$$\Delta G_{EPT} = \Delta G_{Chemical} + \Delta G_{Inter} + \Delta G_{Strain} + G_{Elec} \quad [6.3]$$

The expression for $\Delta G_{Chemical}$ is derived as

$$\Delta G_{Chemical} = G_{\gamma'} - G_{\gamma+B2} \quad [6.4]$$

Where $G_{\gamma'}$, $G_{\gamma+B2}$ are the molar-free energies of γ' and $\gamma + B2$ and these can be expressed in Equations (6.3) and (6.4) in terms of chemical potential (μ) as

$$G_{\gamma'} = \sum_i^{\gamma'} \mu_i X_i \quad [6.5]$$

$$G_{\gamma+B2} = \sum_i \mu_i^{B2} X_i^{\gamma'} \quad [6.6]$$

Where $i = Al, Ni$ and chemical potential of phase can be written in Equation 6.3 as

$$\mu_i^j = G_i^j + RT \ln a_i^j, \text{ Where j} = \gamma', B2 \quad [6.7]$$

Substituting the chemical potential into Equation 8, that gives $\Delta G_{Chemical}$ as

$$\Delta G_{Chemical} = \sum_i X_i^{\gamma'} \left(G_i^{\gamma'} - G_i^{B2} \right) + RT \sum_i X_i^{\gamma'} . \ln \frac{a_i^{\gamma'}}{a_i^{B2}} \quad [6.8]$$

Where μ_i^j is the chemical potential of i^{th} element in j phase, G_i^j is the molar free energy of i^{th} element in j phase, a_i^j is the activity of i^{th} element in j phase, T is the dissolution temperature and R is the gas constant.

Previous studies indicate that interfacial energy (ΔG_{Inter}) and strain energy (ΔG_{strain}) similarly affect temperature, before pulsing and after pulsing, i.e. regardless of electropulsing treatment [154], thus these terms can be neglected in the total free energy change due to electropulsing (ΔG_{EPT}) which can be expressed in Equation 6.9 as

$$\Delta G_{EPT} = \Delta G_{Chem} + \Delta G_{Elec} \quad [6.9]$$

Putting $\Delta G_{Chem} = 0$, in Equation 6.9 that gives the transformation temperature (Te) as

$$Te = -\frac{\sum_i X_i^{\gamma'}\left(G_i^{\gamma'} - G_i^{B2}\right)}{R\ \sum_i X_i^{\gamma'} . \ln\frac{a_i^{\gamma'}}{a_i^{B2}}} \quad [6.10]$$

The molar free energy of the element in the product is higher than that in the parent phase at a temperature lower than the equilibrium temperature (T_e). Now the activity of element in the B2 phase (a_i^{B2}) is greater than the activity of the element in γ' ($a_i^{\gamma'}$). So the nominator $\sum_i X_i^{\gamma'}\left(G_i^{\gamma'} - G_i^{B2}\right) > 0$ and $R\ \sum_i X_i^{\gamma'} . \ln\frac{a_i^{\gamma'}}{a_i^{B2}} < 0$. Therefore, Te is positive.

Similarly, the lowest dissolution temperature (T_{EPT}) under electropulsing, can be obtained by putting $\Delta G_{EPT} = 0$ in Equation 6.9 that gives

$$0 = \sum_i X_i^{\gamma'}\left(G_i^{\gamma'} - G_i^{B2}\right) + RT_{EPT}\ \sum_i X_i^{\gamma'} . \ln\frac{a_i^{\gamma'}}{a_i^{B2}} + \Delta G_{\epsilon lec} \quad [6.11]$$

Now, the T_{EPT} can be expressed in equation 6.12 as

$$T_{EPT} = -\frac{\sum_i X_i^{\gamma'}\left(G_i^{\gamma'} - G_i^{B2}\right)}{R\ \sum_i X_i^{\gamma'} . \ln\frac{a_i^{\gamma'}}{a_i^{B2}}} - \frac{\Delta G_{Elec}}{R\ \sum_i X_i^{\gamma'} . \ln\frac{a_i^{\gamma'}}{a_i^{B2}}} \quad [6.12]$$

Combining Equations (6.10) and (6.12), we get

$$T_{EPT} = Te - \frac{\Delta G_{Elec}}{R\ \sum_i X_i^{\gamma'} . \ln\frac{a_i^{\gamma'}}{a_i^{B2}}} \quad [6.13]$$

The calculated maximum temperature (346°C) under electropulsing conditions, at which dissolution is taking place, is much lower than the dissolution temperature (1242.2°C) as per the equilibrium phase diagram estimated from ThermoCalc.

As $T_{EPT} < T_{e,}$ Equation 6.13 gives that the condition for dissolution of B2 under electropulsing, $\Delta G_{\epsilon lec}$ must be < 0, because the denominator term is < 0.

Now, the free energy (*Ge*) due to electric current can be expressed by using the Maxwell Faraday and Maxwell Ampere laws, in Equation 6.14 [155] as

$$G_{elec} = -\frac{1}{2} \int \vec{\imath} \,.\, \vec{M}\, dr \qquad [6.14]$$

Where $\vec{M}$ is magnetic vector potential inside conductive material, r is a point in real space at which $\vec{\imath}$ is the current density.

Using a general solution of $\vec{M}$ at the given current density $\vec{\imath}$, the free energy G_e due to an electric current distribution can be expressed in Equation 6.15 as

$$G_{\epsilon lec} = -\frac{\mu}{8\pi} \iint \frac{\vec{\imath}(r).\vec{\imath}(r')}{|r-r'|}\, d(r)d(r') \qquad [6.15]$$

The change in free energy ($\Delta G_{\epsilon lec}$) due to a change in current distribution because of electropulsing (due to changes in material, i.e. changes in the conductivity of phases), condition before (0) and after (1), can be expressed in Equation 6.16 [154], [155] as

$$\Delta G_{\epsilon lec} = \frac{\mu}{8\pi} \iint \frac{\vec{\imath_0}(r).\ \vec{\imath_0}(r\prime) - \vec{\imath_1}(r).\ \vec{\imath_1}(r\prime)}{|r-r'|}\, d^3r d^3r' \qquad [6.16]$$

Where r and r' are two distinct locations within the specimen. Equation 20 can be further simplified as [154]

$$\Delta G_{\epsilon lec} = \mu g C i^2 \Delta v \qquad [6.17]$$

Where μ is the magnetic permeability, g is the geometric factor, C is the conductivity coefficient of the alloy, i is the current density and Δv is the volume of dissolved B2. Here,

μ, g, i, and Δv (for dissolution) are positive. The conductivity coefficient (C) is expressed by Equation 6.18.

$$C = \frac{\sigma_2 - \sigma_1}{\sigma_1 + 2\sigma_2} \quad [6.18]$$

Here, σ_1 is the electrical conductivity of the product phase (γ'), σ_2 is the electrical conductivity of the parent phase mixture ($\gamma + B2$).

Now, EDS analysis of phases in samples without electropulsing reveals that B2 bands are much enriched with Ni and Al by 10% and 7%, respectively in comparison to those in the austenite matrix. As per Matthiessen's theory, the resistivity of B2 bands is much higher than that of the austenite. In other words, the electrical conductivity of B2 is lower than that of austenite. As a result, the conductivity coefficient C is less than zero. Therefore, from the change in free energy due to electrical current (ΔG_{Elec}) is also < 0. Substituting $\Delta G_{Elec} < 0$, in Equation (6.9) and combining the Equations (6.4) and (6.6) gives $T_{EPT} < T_e$. Therefore, thermodynamic calculations suggest that electropulsing treatment may lead to the dissolution of B2 at a much lower temperature than the dissolution temperature under thermal equilibrium. Dissolution takes place at high temperatures and high activation which is expected during the initial few peaks of damped oscillations of electropulsing. As a result, refinement (geometrically) of banded, globular, and platelet B2 phases takes place during the initial few peaks. Local dissolution disintegrates platelets into smaller ones as shown in Figure 6.1d and f.

6.2.2.4.2 Deformation and fragmentation

During electropulsing, under high voltage, electrons move as electron wind with kinetic energy. It exerts a dynamic force on atoms/dislocations on impact and transfers momentum and energy. This dynamic force is regarded as electron wind force, and the transferred energy serves as the primary driving energy behind the changes in structure/microstructure and properties of the alloy. The high-energy atoms/dislocations (groups of atoms) undergo

transportation along the direction of the electric current. When high voltages are applied, the flow of electrons can be vigorous, and the wind force (F_{ew}) exerted by the electron wind on dislocations (force per unit dislocation length) is determined by Conrad and is given by the Equation 6.19 [156]:

$$F_{ew} = \frac{I\rho c_e n_e}{\rho_{hkl}} \quad [6.19]$$

Where c_e is electron charge, n_e is electron density and ρ_{hkl} is the dislocation density. Taking I as $7.5*10^9$ A/m^2 (first peak of waveform of electropulsing), c_e as $1.60217663 \times 10^{-19}$ C, $n_e = 5.3*10^{29}$/m^3 and L= $0.08*10^{15}$/m^2, the electron wind force is calculated to be 2.2 N/m. Peach and Koehler have correlated the uniform force (F) acting perpendicular to a straight dislocation of unit length, with critical resolved shear stress component (τ) on slip plane resolved in the direction of the Burgers vector (b), and the relation is given by the Equation 6.20 [157].

$$F = \tau b \quad [6.20]$$

Taking Burger's vector as 2.6 Å, the shear stress acting upon the dislocation due to electron wind force (τ) is calculated to be 8.5 GPa. Critical resolved shear stress acting on dislocation upon yielding is calculated from the yield strength (1015 MPa for PD3-A low-density duplex steel) to be 0.51 GPa. Considering the hardness of the B2 phase, i.e., 6.9 GPa [80], the yield strength of B2 would be approximately 2.3 GPa, which is still lower than the shear stress applied by the electron wind force. Therefore, plastic deformation of the material is likely to occur during the first peak or initial few peaks of the waveform of electropulsing, and the presence of α-fiber texture component in the B2 phase at $\varphi2 = 45^\circ$ sections provides evidence that the plastic deformation is taking place in B2 phase. To further substantiate the occurrence of B2 fragmentation, the theoretical fracture strength of B2 is computed with the elastic modulus (E) as 162 GPa, surface energy (γ_s) as 0.5 J/m² [158], and interatomic distance (α_0) as 2.90 Å using Equation 6.21.

$$\sigma_{th} = \sqrt{\frac{E\gamma_S}{a_0}} \quad [6.21]$$

The calculated fracture strength of the B2 phase is found to be 16.6 GPa.

However, conventionally produced materials cannot attain such high fracture strength due to factors like dislocations, residual stresses, and internal cracks. Generally, it is proposed that theoretical shear strength values are around 1/200 times the elastic modulus. Therefore, the fracture strength is estimated to be 0.8 GPa, which is an order of magnitude lower than that of applied shear stress through electron wind force to dislocations that exert stress on B2 by piling up in austenite. Hence, the fragmentation of B2 is likely to occur. The cracks found on B2 bands are experimental evidence of this fragmentation (Figure 6.1 (b)).

6.2.2.4.3 Precipitation

During the later part of electropulsing, sample temperature goes down rapidly, and the material becomes supersaturated but the rise in temperature and electrical free energy available for transformation is low due to low current density. The reduction in barrier-free energy for phase transformation like precipitation due to electric current is again ΔG_{Elec}. The expressions for ΔG_{Elec} are given by Equations 6.16 and 6.17 but here, σ_1 is the electrical conductivity of the product phase mixture ($\gamma + B2$), σ_2 is the electrical conductivity of the parent phase (γ'), thereby C < 0, and $\Delta G_{Elec} < 0$. The temperature rise and reduction in barrier energy, are sufficient for the precipitation process at low temperatures. Therefore, additional fine size platelets and spheroidized precipitates have formed due to electropulsing (Figure 6.1(f)).

The instantaneous increase in temperature caused by electropulsing generates a significant number of vacancies within the material. These vacancies originate from interfaces, grain boundaries, and dislocations. The migration of these vacancies within the solid solution is enhanced compared to conventional aging temperatures due to the additional energy

provided by the electron wind force. The force exerted by the electron wind generates a higher number of dislocations. The vacancies and dislocations act as nucleation sites for precipitation.

Hans Conrad showed that an electric current density greater than 10^3 A/mm^2 can speed up the solid-state phase transformation in alloys by accelerating atomic diffusion. The measured peak-current density ranges between 7.5 kA/mm^2 to 0.26 kA/mm^2 which are much above 10 A/mm^2. At high current density when a rise in temperature (as described in section 4.1.2, 346°C) and reduction in activation energy (section 6.3.4.1) are high dissolution of B2 precipitates takes place. After the partial dissolution of B2, nickel and aluminum content in austenite increases. As electropulsing tends to increase the conductivity of the material, it tries to reduce the resistivity of austenite by precipitating out B2 through the electromigration phenomenon which is accelerated atomic motion/diffusion in a metal under an applied electric field [159]. The atomic drift flux *(Φ)* is given by Equation 6.22 [156] as the Nernst-Einstein equation.

$$\Phi = \frac{ND}{kT}\rho ieZ^* \qquad [6.22]$$

Where *N* is the density of solute atoms, *D* is the diffusion coefficient, *k* is the Boltzmann constant, and *Z** is the effective valence of the solute atom.

Thermodynamically, when high-energy electron wind force interacts with dislocations, electrons get scattered unevenly and cause an anisotropic shielding effect, which reduces the kinetic barrier. The diffusion coefficient of atoms can be expressed as

$$\mathrm{D} = D_0 \exp\left(-\frac{Q_{eff}}{KT}\right) \qquad [6.23]$$

Where D_0 is the pre-exponential constant, Q_{eff} is the effective activation energy.

Here, $Q_{eff} = Q - \Delta Q_{athermal}$, $\Delta Q_{athermal}$ is the magnitude of reduction in activation energy due to athermal effects, K is the Boltzmann constant and T is the absolute

temperature. This decrease in the barrier increases the mobility of atoms thereby increasing the diffusivity and enhancing the precipitation.

The dislocations generated by electropulsing also enhance diffusion by providing fast paths for atoms, known as pipe diffusion [160]. This pipe diffusion can increase the diffusion of atoms by three times compared to bulk diffusion thereby enhancing the precipitation [161]. A slight increase in the volume fraction of B2 precipitation is observed, possibly attributed to the enhanced mobility of nickel towards aluminum, given their higher affinity [162]. Additionally, the increased kinetics of precipitation, influenced by electropulsing at lower temperatures [163], [164], is noted. The precipitation-free zone near coarse precipitate is a result of a lack of nucleation sites like vacancies and dislocations that have migrated to nearby boundaries [103].

As a result of accelerated diffusion, and reduction in barrier energy, electropulsing also enhances the nucleation rate of precipitation of B2. The accelerated nucleation rate (Ie) can be given by Equation 6.24 [103].

$$I_e = I_0 \left(\frac{D}{\lambda^2}\right) \exp\left(-\frac{\Delta G_0 + \Delta G_{Elec}}{kT}\right) \quad [6.24]$$

Where, I_0 is a constant, λ is jump distance, ΔG_0 is the nucleation barrier of B2 without electropulsing, the nucleation rate without electropulsing (I) can be given as,

$$I = I_0 \left(\frac{D}{\lambda^2}\right) \exp\left(-\frac{\Delta G_0}{kT}\right)$$

6.2.2.4.4 Spheroidization

The concentration of austenitic matrix in equilibrium with small size precipitate is dependent on the radius of curvature and the variation of concentration with a change in radius due to the Gibbs-Thomson effect is expressed in Equation 6.25 as

$$C_i^{r1} - C_i^{r2} = \frac{2V_m C_{io} \gamma_S}{RT}\left(\frac{1}{r1} - \frac{1}{r2}\right) \quad [6.25]$$

Where C_i^{r1}, C_i^{r2} corresponds to the concentration of ith element in austenite in equilibrium with precipitate at two different radii of $r1, r2$, respectively, of B2 precipitate, V_m is the molar volume, C_{i0} is the concentration of ith element in austenite in equilibrium with a large-sized precipitate. Due to the concentration gradient in austenite close to small size precipitate, elements in austenite move to lower concentration region which is near a higher radius, i.e. flat surface. To maintain the equilibrium, the regions of the low radius of B2 precipitate, i.e. sharp areas, dissolve, and the elements from austenite deposit on flat areas of the precipitate. As a result, the small nonspherical precipitates get spheroidized (Figure 6.1(f)).

6.2.2.4.5 Recrystallization

Recovery and recrystallization are strong functions of the amount of defect density. The static recrystallization temperature of austenite in duplex low-density steel of similar type is reported to be greater than 900°C [165]. The recrystallization temperature of B2 is much higher than the above. The thermal effect of electropulsing can raise the maximum temperature to 346°C. Therefore, the thermal energy is insufficient to recrystallize either austenite/B2. The athermal part of the electrical energy of electron wind reduces the required activation energy and allows recrystallization at a much lower temperature. As a result, the selected electropulsing parameters can recrystallize only a few localized areas where dislocation density in the matrix is high i.e. near banded B2. As a result, dislocation density in recrystallized areas is low, KAM values are reduced but MA is increased. Electropulsing of selected steel can recover dislocations in B2. At high current density, deformation in B2 or in austenite takes place due to pushing of dislocations by electron wind force which raises dislocation density but simultaneously dislocations are also annihilated in B2 by recovery but in austenite by recrystallization. Annihilation is dominating over deformation/generation of dislocations. As a result, lower dislocation

density is recorded in both B2 and in austenite. LAGB fraction in B2 is increased, and dislocation density is reduced by an order of magnitude. Average MA values are also reduced. Based on the above-resulted mechanisms, a physical model of microstructural developments is shown in Figure 6.9 (a-d). Figure 6.9(a) depicts schematic features in the microstructure of PD3-A. The microstructure consists of banded B2 (1, 2, 3, 8), globular B2 (4, 5, 10), B2 platelets (6, 7), and recovery of austenite (9). Figures. 6.9(b-d) display model features of different stages due to electropulsing. At high current density of the pulse, dissolution (1^{I}-8^{I}, 10^{I}) partial dissolution/disintegration (6^{I}, 7^{I}), deformation and fragmentation (8^{I}) of B2 take place (Figure 9(b)), spheroidization (1^{II}-8^{II}, 10^{II}), and nucleation of recrystallized austenite (9^{II}) (as shown in Figure 6.9(c)). At lower current density, electropulsing drives precipitation of B2 platelets (11), spheroidization of B2(1^{III}-8^{III}, 10^{III}) and growth of recrystallized austenite (9^{III}) (Figure 6.9(d)).

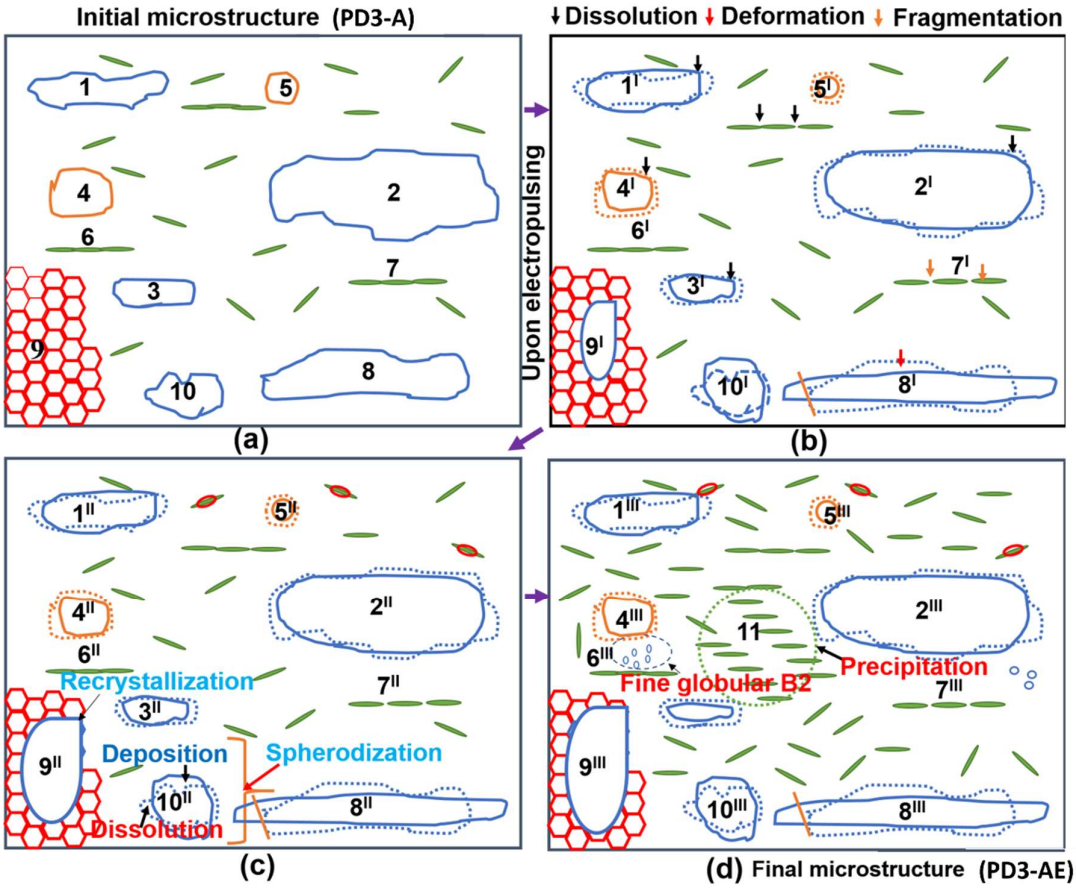

Figure 6.9: Physical model of microstructures of (a) PD3-A, B2 bands(1, 2, 3, 8), globular B2 (4, 5, 10), B2 platelets (6, 7), recovery of austenite (9), different stages after electropulsing, PD3-AE, (b) dissolution of B2 (1l-8l, 10 l), the disintegration of B2 spheroidization(10^{l}) of B2, sublimation of austenite subboundary (9^{l}), (c) spheroidization (1^{ll} -8^{ll}, 10^{ll}), nucleation of recrystallized austenite (9^{ll}), and (d) precipitation of B2 platelet (11)., spheroidization of B2 (1^{lll} -8^{lll},10^{lll}) and growth of recrystallized austenite (9^{lll}). In Figure b-d, dotted boundaries are original boundaries and solid boundaries are boundaries after electropulsing.

6.2.2.5 Texture

The texture of B2 in the PD3-A steel (Figure 6.6(a)) primarily exhibits rotated cube components, potentially arising from the transformation of cube components of recrystallized austenite grains during the annealing treatment, that is, the formation of B2 precipitates from recrystallized austenite [166]. The formation of the α-fiber texture

component can be due to the deformation induced by the higher critical resolved shear stress because of electron wind force in the PD3-AE sample. Thermal as well as athermal energy is not sufficient for the recrystallization of B2.

The texture of austenite in PD3-A steel (Figure 6.6(c)) primarily shows the presence of Goss, A, Goss twin, and S components. The Goss and A components pertain to the α-fiber, the Goss twin belongs to the τ-fiber, and the S component belongs to the β-fiber [167]. This suggests that after annealing the material at 930°C, the austenite grains also do not recrystallize and retain the deformed austenite rolling texture. In PD3-AE, the Goss texture components are eliminated, and the intensity of A components has increased by 1R compared to the PD3-A sample. (Figure 6.6 (d)). S component and Goss twin components are also completely dissolved. After electropulsing of PD3-AE also, there is an absence of cube texture components in the ODF sections of the austenite phase, a primary recrystallization texture component for FCC materials. This suggests that recrystallization did not occur in the current scenario in austenite, potentially due to strong inhibition from the alloying elements and B2 precipitates.

6.2.2.6 Work hardening behavior

Figure 6.10(a) presents the plots of logarithmic true stress versus logarithmic true plastic strain for PD3-A and PD3-AE samples, clearly demonstrating an upward concave shape in each condition. There are approximately two types of change in slopes or work hardening rates, one at low strain and the other at high strain, with a transition at intermediate strain. To find work hardening parameters, experimental logarithmic true plastic stress vs logarithmic true plastic strain plot is fitted with the flow curves based on various models of Hollomon [109], Ludwik [110], Ludwigson [112], Swift [111], and Voce [113]. Figures. 6.10 (b), and 6.10 (c) depict the superimposed curves derived from the models and experimental flow curves of PD3-A and PD3-AE samples, respectively. Among the

various models considered, the Ludwigson relationship was found to be the best fit for the experimental data, as evidenced by the highest R^2 values and the lowest ξ^2 values.

Ludwigson flow behaviour is given by Equation 6.26.

$$\sigma = exp(K_1 + n_1\varepsilon) + K_2\varepsilon^n \quad [6.26]$$

Where K_1 and K_2 are strength coefficients and n_1, and n_2 are work-hardening exponents, respectively, at low and high strain regimes but before necking.

Table 6.2 provides the R^2 values, ξ^2 values, and other work-hardening parameters for the Ludwigson flow equation of PD3-A and PD3-AE. As seen from Table 1, the strength coefficients exp(K_1) of PD3-A and PD3-AE at low strain regimes are positive but almost the same (916 or 1064 MPa, respectively). The respective work-hardening exponents (n_1) are -1.60 and -0.44. At a high strain regime both the strength coefficient (K_2) 1651 and work hardening exponent (n_2) 0.75 of PD3-AE are higher than that of the respective parameters 575 and 0.30 of PD3-A. As a result, the ultimate tensile strength of the electropulsed sample (PD3-AE) is much higher than that of the annealed one (PD3-A).

Differentiation of Ludwigson equation with respect to strain is given by Equation 6.27 which provides the changes in work hardening rate.

$$\frac{d\sigma}{d\varepsilon} = n_1 \exp(K_1 + n_1\varepsilon) + K_2 n_2 \varepsilon^{n_2 - 1} \quad [6.27]$$

Equation 6.27 clearly states that there are two types of changes in work hardening rate with respect to true strain. Considering the strength coefficients and work hardening exponents, at a low strain regime, work hardening rates rapidly but at a higher strain regime, it decreases slowly. Figure 6.10(d) illustrates the variation in experimental work hardening rate with respect to true plastic strain for both PD3-A and PD3-AE samples in three stages (Stage 1-Stage 3). The initial transient stage is characterized by a sharp decrease in the work hardening rate, Stage 2 at which the work hardening rate remains nearly constant, and Stage 3 at which the work hardening rate also reduces rapidly. The initial higher value

of work hardening in the annealed sample, compared to the electropulsed sample can be attributed to its higher dislocation density [168]. This observation indirectly supports the assertion that the dislocation density of the electropulsed sample decreases, as determined by XRD analysis. As explained by Equation 6.27, at a low strain regime, (~0-0.02) work hardening rate decreases rapidly with gradients of -320 GPa and -190 GPa, respectively for PD3-A and PD3-AE. Stage 1 typically arises due to the planar flow of dislocations over relatively long distances, where dislocations encounter minimal obstacles such as precipitates or grain boundaries that impede their motion [146]. In this transient stage, also known as the easy glide stage, as stress increases, both dislocation velocity and density rise, resulting in a rapid increase in plastic strain rate [169]. At higher strain regimes (~0.02 -0.14) work hardening rate decreases gradually though there are small humps and dips present. The gradients of the work hardening rate with respect to true strain are -9.5 GPa and -7.4 GPa, respectively, for PD3-A and PD3-AE. As it is generally understood that materials with high stacking fault energy facilitate easy cross-slip, there is minimal resistance offered by precipitates, owing to their coarser size. Consequently, this leads to a steady slope in stage 2, as illustrated in the curves of PD3-A and PD3-AE samples. However, in comparison with PD3-A, PD3-AE sample exhibit more pronounced dips and humps, attributed to the resistance posed by the presence of fine-sized B2 precipitates resulting from the electropulsing treatment. The activation of cross-slip and multiple slip systems promotes the development of heterogeneous dislocation structures, characterized by dislocation tangles, walls, and cells, the fraction of which escalates with increasing plastic strain during stage 2 [125]. Stage 2 corresponds to the phase of increased dislocation storage, marked by the proliferation of wall and cell structures, leading to a rise in dislocation density.

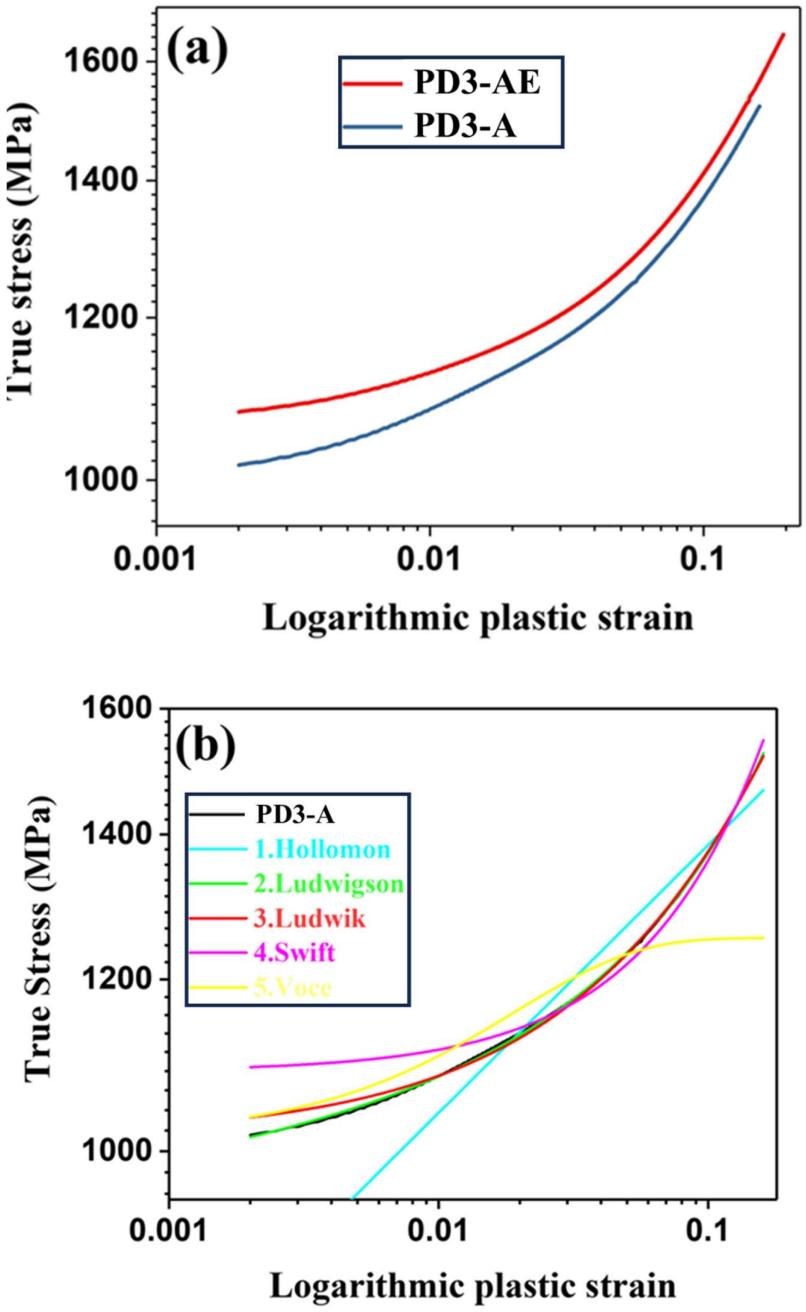

Figure 6.10: Logarithmic true stress vs. logarithmic true plastic strain plots of PD3-A and PD3-AE samples (a) experimental, (b) &(c) experimental fitted with Hollomon, Ludwik, Ludwigson, Swift and Voce models and (d) work hardening rate vs true plastic strain diagrams for PD3-A and PD3-AE. Electropulsing reduces work hardening rate but increases ductility but decreases recovery.

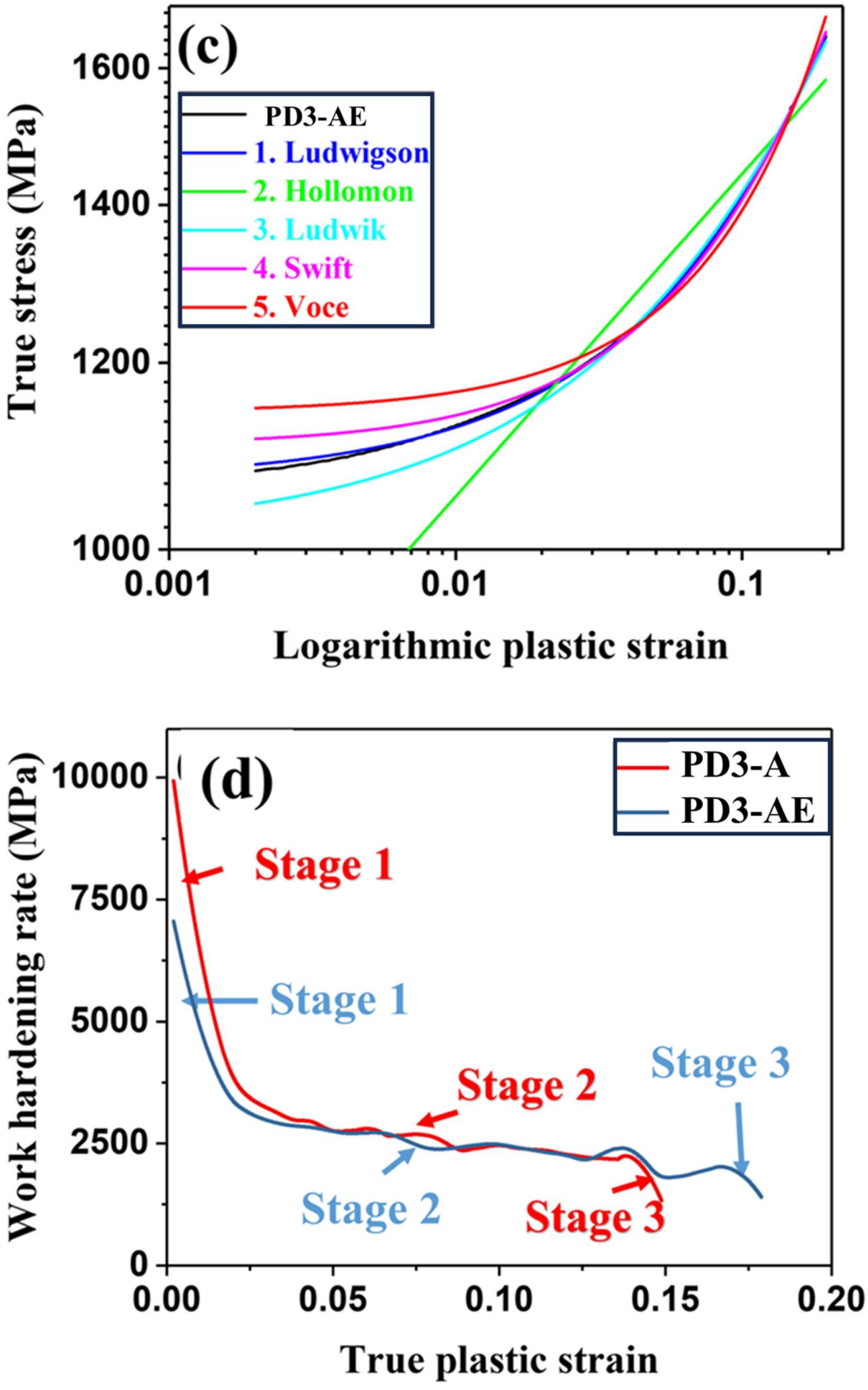

Figure 6.10. Continued.

Table 6.2: Work hardening parameters.

Sample	exp(K_1) (MPa)	n_1	K_2 (MPa)	n_2	R^2	ξ^2
PD3-A	916	-1.60	575	0.30	0.9998	2.2564
PD3-AE	1064	-0.44	1651	0.75	0.9999	1.9123

Stage 3 corresponds to the dynamic recovery process, during which dislocations undergo annihilation, resulting in a decrease in the work hardening rate. The linear relationship observed between the hardening rate ($\frac{d\sigma}{d\epsilon_p}$) and true plastic strain (ϵ_p) curves in the third stage (Figure 6.10(d)) can be most effectively elucidated similar to the Kock, Mecking, (KM) dislocation models : [118], as expressed in Equation 6.28.

$$\frac{d\sigma}{d\epsilon} = \theta_0 + m\varepsilon \qquad [6.28]$$

Here, $\frac{d\sigma}{d\epsilon}$ and ε represent the strain hardening rate and the true strain, respectively. θ_0 is the initial work-hardening rate which represents the athermal mobile dislocations storage that has become immobilized after traveling a distance proportional to the average slip spacing. The term m corresponds to the slope of the linear regimes associated with the annihilation of dislocations due to cross slip during dynamic recovery [127]. A high value of θ_0 indicates a high dislocation storage capacity signifying the material's ability to retain dislocations. Conversely, a high negative value of m suggests high dynamic recovery implying that the material experiences work softening.

The results of the linear fitting for the third stage of both PD3 and PD3-A samples are depicted in Figure 6.11. The Adjusted R^2 value of the fitted curves is nearly 1, which indicates a very high correlation between the experimental data and the fitted curve. The

dislocation storage capacity (θ_0) of PD3-A and PD3-AE are found to be 31 GPa and 14 GPa, respectively.

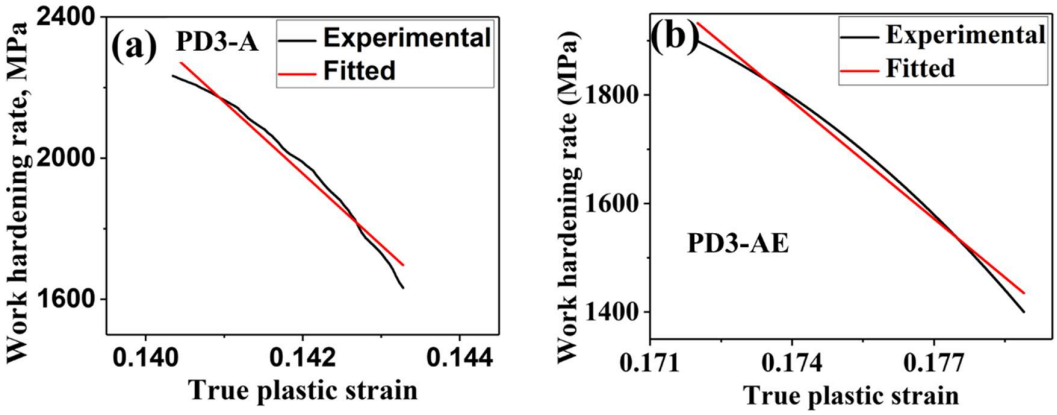

Figure 6.11: Linear fitting curves of (a) PD3-A and (b) PD3-AE samples using Kock, Mecking (KM) based dislocation models.

This suggests that PD3-A has a higher dislocation storage capacity compared to PD3-AE. On the other hand, the negative slope (m) of the curve for PD3-A and PD3-AE are observed to be -203 GPa and -72 GPa, respectively. This suggests that PD3-AE has a lower dynamic recovery compared to PD3-A.

The improved ductility observed in duplex low-density steel subjected to electropulsing treatment can be attributed to spheroidization as well as refinement of B2 and a decrease in the dislocation density in the matrix. The reduction in dislocation density may be attributed to the deformation strain imposed by the electron wind force, as elucidated in section 6.4.3.2. In the process of plastic flow, dislocations within the matrix are rearranged, leading to a decrease in dislocation density. Previous literature has also demonstrated a decrease in dislocation density through electropulsing [170], [171]. Xiang et al. demonstrated that dislocations-oriented perpendicular to the direction of drift electrons either progress toward the grain boundary or undergo annihilation during their movement. In contrast, dislocations aligned parallel to the direction of drift electrons remain

unchanged and straighten due to the influence of the electron wind force [172]. Moreover, they demonstrated that the ability of the Frank-Read source to generate dislocations under the influence of the electron wind force diminishes. Consequently, while dislocations perpendicular to the direction of the wind flow are being annihilated in one direction, dislocations in the other direction are not being generated. This results in an overall reduction in dislocation density. As a result, the plasticity of the PD3-A sample increases by 5.3% after electropulsing. Both the samples PD3-A and PD3-AE have ductile austenite and brittle B2 precipitates. Therefore, both samples fail by ductile-brittle fracture as confirmed by the presence of dimples and cleavage facets. Facets are originated by large size B2 or banded B2. Electropulsing decreases the size and volume fraction of banded B2. Therefore, the area fraction of facets is decreased in PD3-AE. On the other hand, the area fraction of dimples is increased. As a result, the electropulsed sample reports higher ductility.

6.3 Effect of electropulsing treatment on PD3-AB$_{30}$

6.3.1 Results

The microstructure of PD3-AB$_{30}$ steel depicts the presence of the banded B2 phase with an average width of 8.3 ± 1.8 μm and length of 36 ± 10 μm (Figure 6.12 (a)), B2 platelets with a width of 0.09 ± 0.03 μm, and the length of 0.45 ± 0.09 μm (Figure 6.12 (b)), and globular B2 structure of average diameter of 0.93 ± 0.4 μm (Figure 6.1 (b)) are observed within the austenitic matrix. After electropulsing treatment, B2 precipitate morphologies are refined. The width of banded, platelet B2 reduces to 5.65 ± 1.2 μm and 0.08 ± 0.03 μm (Figure 6.12 (c), (d)) respectively. On the other hand, the length of bands and platelets are also reduced to 27.1± 8.0 μm, and 0.33 ± 0.05 μm (Figure 6.1 (c), (d)). The diameter of globular B2 is

also decreased to 0.81 ± 0.16 µm (Figure 6.1 (d)). Table 6.3 presents the sizes of B2 bands, B2 platelets, and globular B2 particles before and after electropulsing treatment.

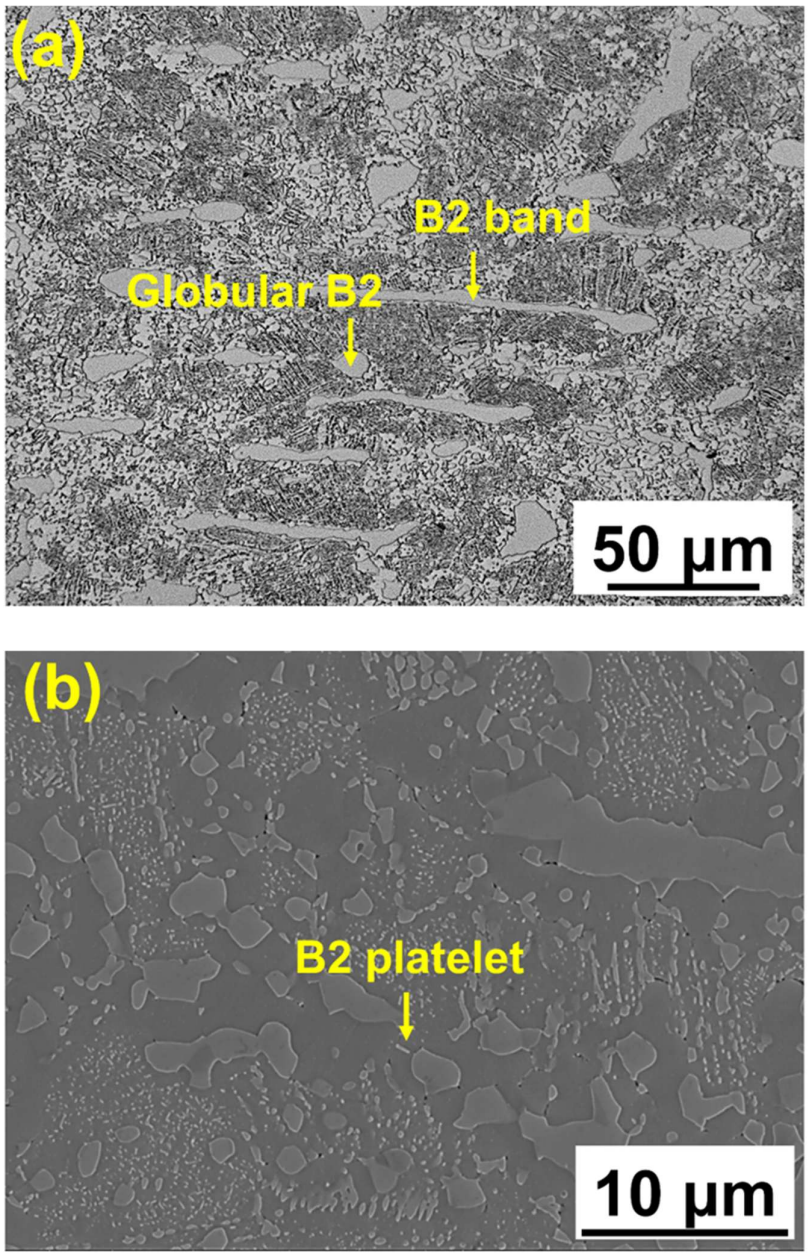

Figure 6.12: (a) Optical micrograph, (b) secondary electron micrograph of PD3-AB_{30} sample depicting B2 platelets, globular B2 and banded B2 structures (as indicated by yellow arrows) in austenite matrix, (c) optical micrograph displaying deformed and fragmented B2 (d) secondary electron micrograph of PD3-AB_{30}E sample showing disintegrated B2 and B2 precipitate.

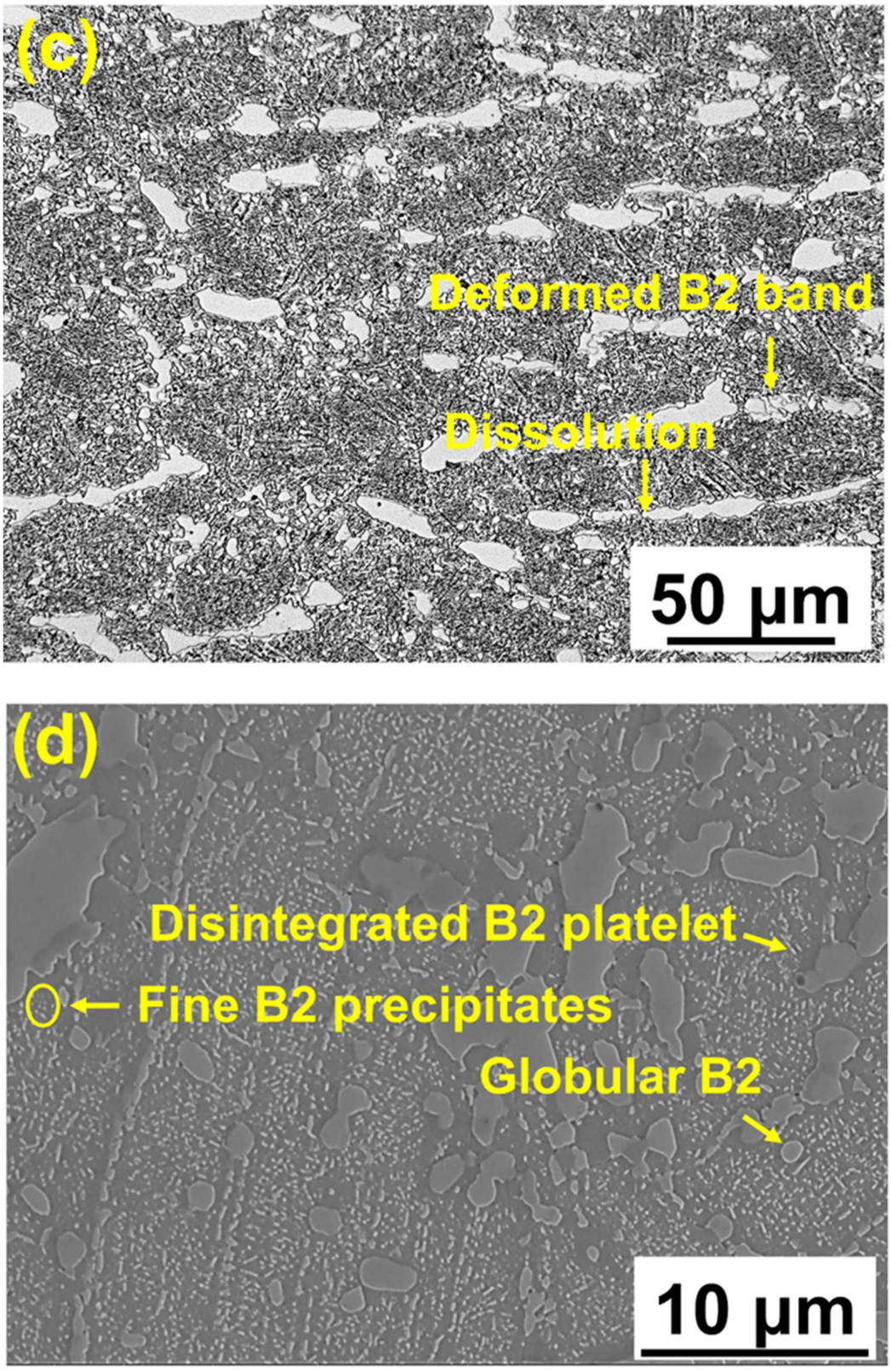

Figure 6.12. Continued.

Table 6.3: Sizes of different B2 morphologies before and after electropulsing.

B2 morphology	Size Before Pulsing (μm)		Size after pulsing (μm)	
	Length	Width	Length	Width
B2 Band	36 ± 10	8.3 ± 1.8	27.1± 8.0	5.65 ± 1.2
B2 platelet (SEM)	0.45 ± 0.09	0.09 ± 0.03	0.33 ± 0.05	0.08 ± 0.03
Globular B2(SEM)	0.93 ± 0.4		0.81 ± 0.16	

The XRD patterns of the PD3-AB_{30} and PD3-AB_{30}E samples, confirming the presence of austenite, B2, kappa carbide, and alpha ferrite phases (Figure 6.13). In the PD3-AB_{30} sample, the volume fractions of austenite, B2, kappa carbide, and alpha ferrite are 71%, 21%, 3%, and 5%, respectively. After electropulsing treatment, these values change to 74%, 19%, 1.5%, and 5.5%, respectively. The increase in the austenite volume fraction, alongside the reduction in B2 and kappa carbide fractions, have been observed in case of PD3-AB_{30}E sample. The dislocation densities for austenite and B2 phases in the PD3-AB_{30} sample are 3.8×10^{14} m^{-2} and 5.6×10^{14} m^{-2}, respectively. After electropulsing treatment, in the PD3-AB_{30}E sample, the dislocation densities decrease to 2.62×10^{14} m^{-2} for austenite and 4.52×10^{14} m^{-2} for the B2 phase. The volume fractions of various phases and the calculated dislocation densities for the austenite and B2 phases (Table 6.4).

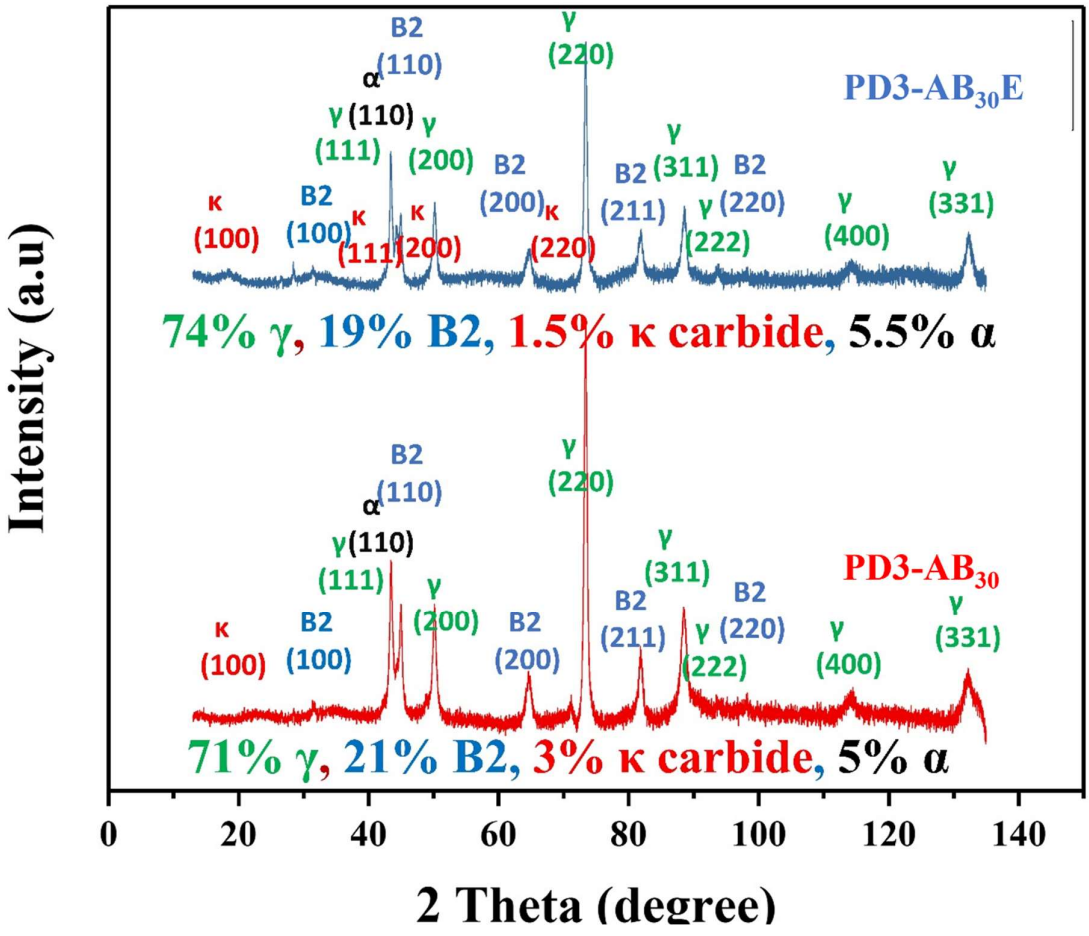

Figure 6.13: XRD patterns of PD3-AB_{30} sample and PD3-AB_{30}E samples conforming the presence of austenite and ordered B2 phase, kappa carbide phases.

Table 6.4: Volume fraction and dislocation density values of PD3-AB_{30} and PD3-AB_{30}E samples.

Materials	Volume percent phases (%)	Dislocation density ($x10^{14}/m^2$)	
		γ	B2
PD3-AB_{30}	71% γ, 21%B2, 3% k-carbide, 5%α	3.8	5.6
PD3-AB_{30}E	74%γ, 19%B2, 1.5% k-carbide, 5.5% α	2.62	4.52

TEM bright-field (BF) images of the PD3-AB_{30} and PD3-AB_{30}E samples, illustrating distinct microstructural differences before and after electropulsing treatment. In the PD3-AB_{30} sample, lamellar kappa carbide and ferrite structures are visible, characteristic of the as-processed microstructure (Figure 6.14 (a)). In contrast, the PD3-AB_{30}E sample shows fragmented kappa carbide particles, indicating the effect of electropulsing in modifying the morphology of kappa carbide (Figure 6.14 (b)).

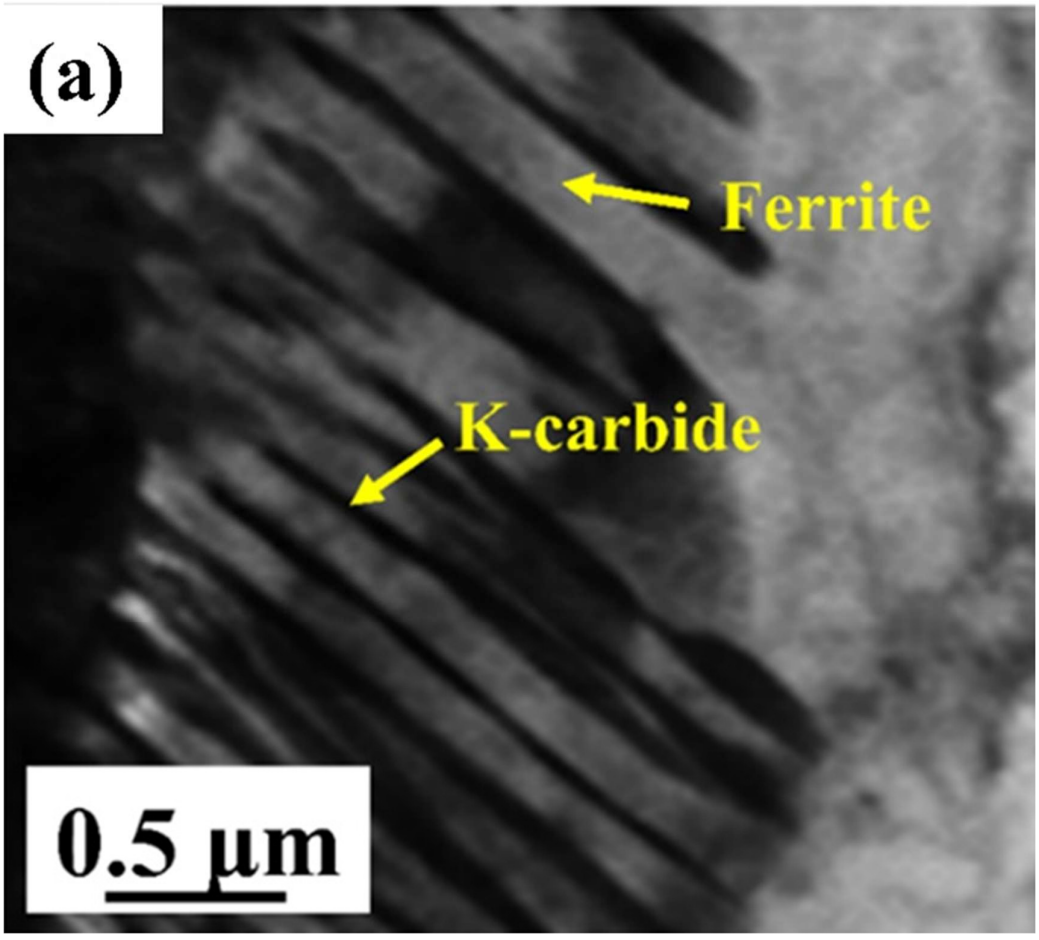

Figure 6.14: TEM BF images of (a) PD3-AB_{30} and (b) PD3-AB_{30}E samples.

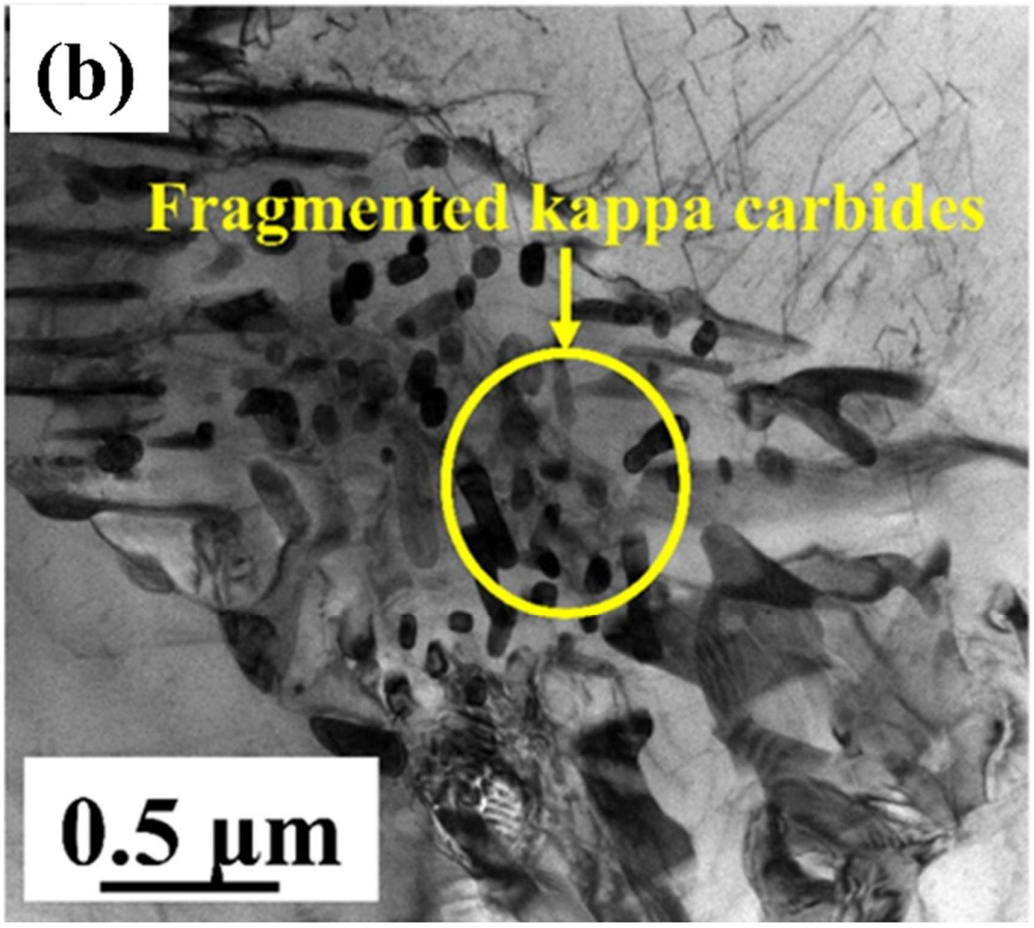

Figure 6.14. Continued.

Image quality (IQ) maps for the B2 phase with superimposed grain boundaries in PD3-AB_{30} sample presents that, low-angle grain boundaries (LAGBs) constitute 39.3% and high-angle grain boundaries (HAGBs) make up 60.7% (Figure 6.15 (a)). In the PD3-AB_{30}E sample, these fractions shift to 31.3% LAGBs and 67.7% HAGBs, indicating an increase in HAGBs likely due to dislocation rearrangement induced by electropulsing. For the austenite phase, the LAGB and HAGB fractions in PD3-AB_{30} are 76% and 24%, respectively. In PD3-AB_{30}E, the LAGB fraction decreases to 64.5%, while the HAGB fraction rises to 34.5%, suggesting that LAGBs have coalesced into HAGBs as a result of the electropulsing treatment.

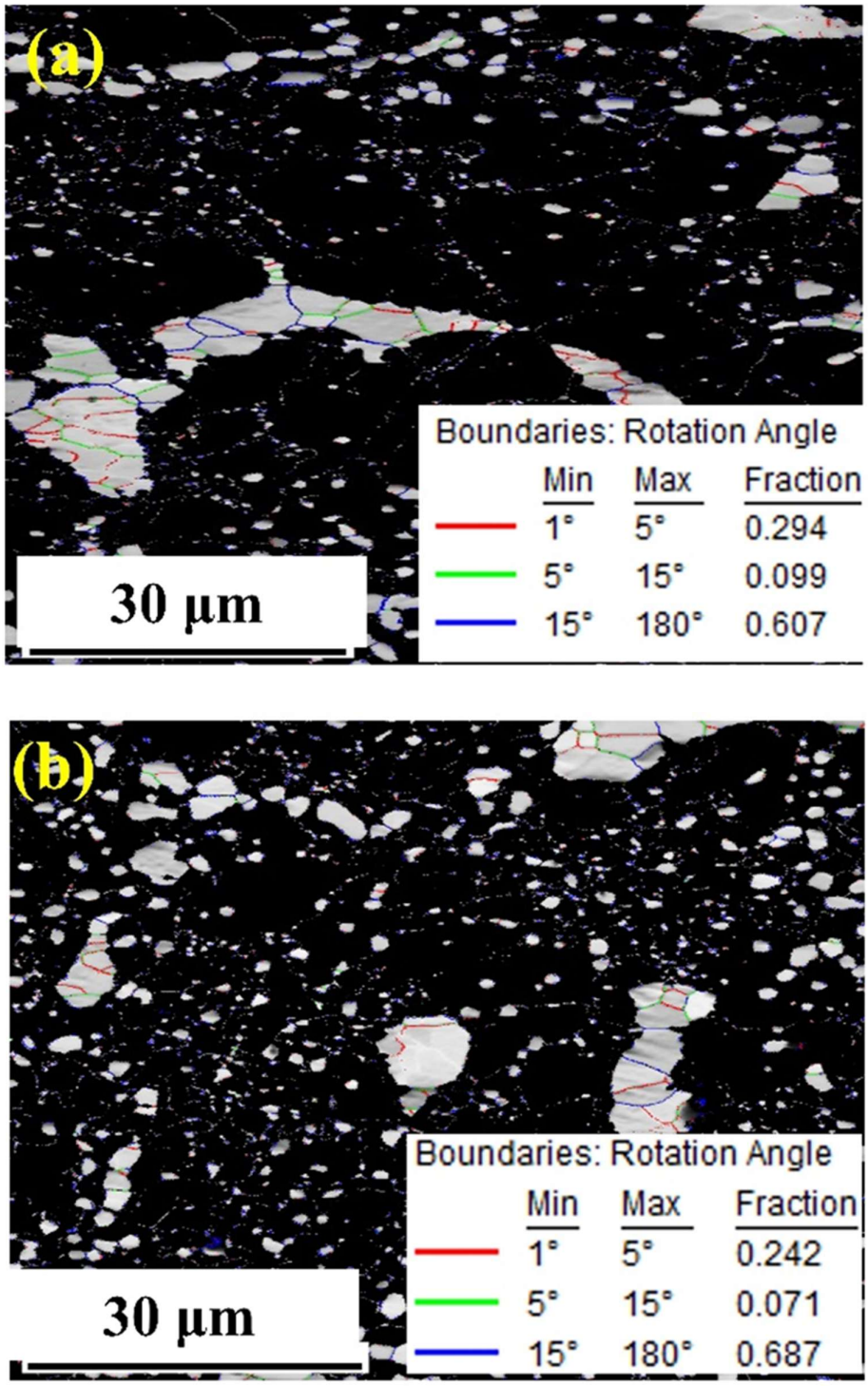

Figure 6.15: Image quality map with superimposed grain boundaries of (a) B2 (c) austenite in PD3-AB_{30} sample, (b) B2 (d) austenite in PD3-AB_{30}E sample (the fraction of LAGB of misorientation angle <15° and HAGB of misorientation angle >15° are shown in inset).

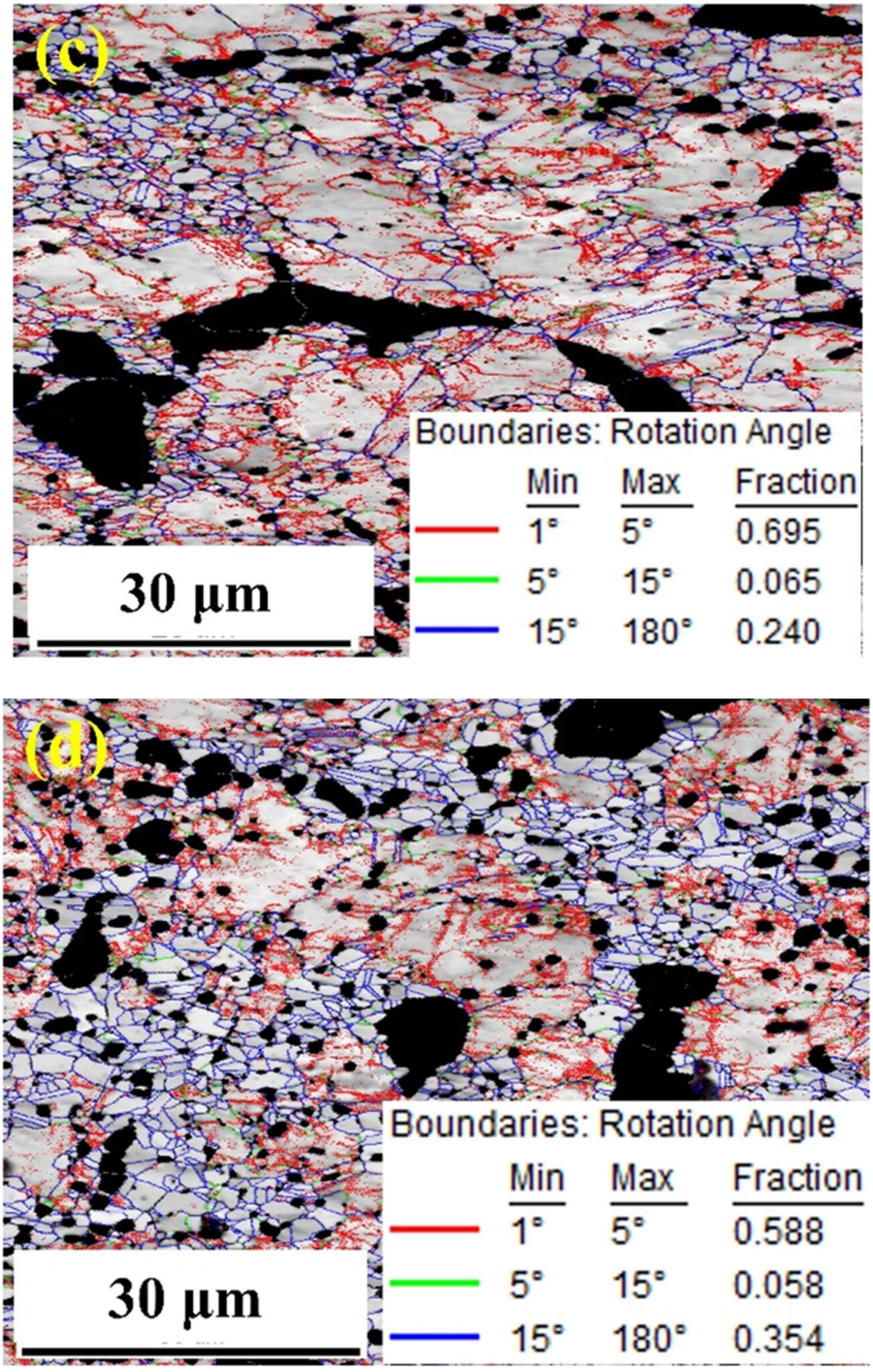

Figure 6.15. Continued.

The number fraction versus misorientation angle (MA) for the B2 For the B2 phase, the average MA increases from 26.2° in PD3-AB_{30} to 29.7° in PD3-AB_{30}E, while for the austenite phase, the MA rises from 13° to 19° indicating recrystallization ((Figures 6.16 (a), (b))). The kernel average misorientation (KAM) maps of the B2 phase shows that the PD3-AB_{30} sample has an average KAM value of 0.65° (Figure 6.17(a)), which decreases slightly to 0.62° in the PD3-AB_{30}E sample (Figure 6.17(b)). Similarly, the austenite phase shows a reduction in average KAM values from 0.59° in PD3-AB_{30} (Figure 6.17(c)) to 0.56° in PD3-AB_{30}E (Figure 6.17(d)). These reductions in KAM values suggest a decrease in localized strain following electropulsing treatment, indicating stress relaxation and potential recovery effects in both phases. LAGB and HAGB fractions, and average MA and KAM values of B2 and austenite are presented in Table 6.5.

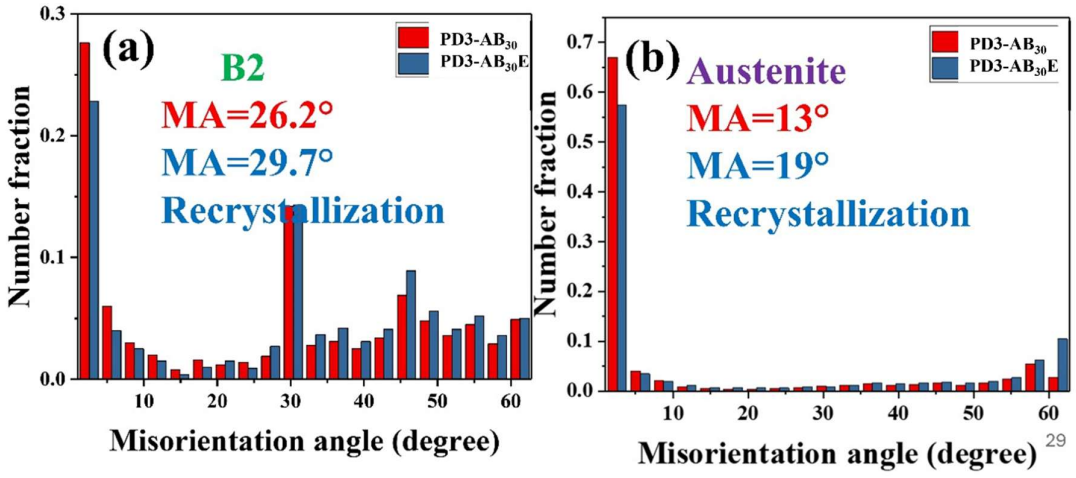

Figure 6.16: Number fraction vs misorientation angle of (a) B2 and (b) austenite in both PD3-AB_{30} and PD3-AB_{30}E samples. B2 and austenite phases are partially recrystallized.

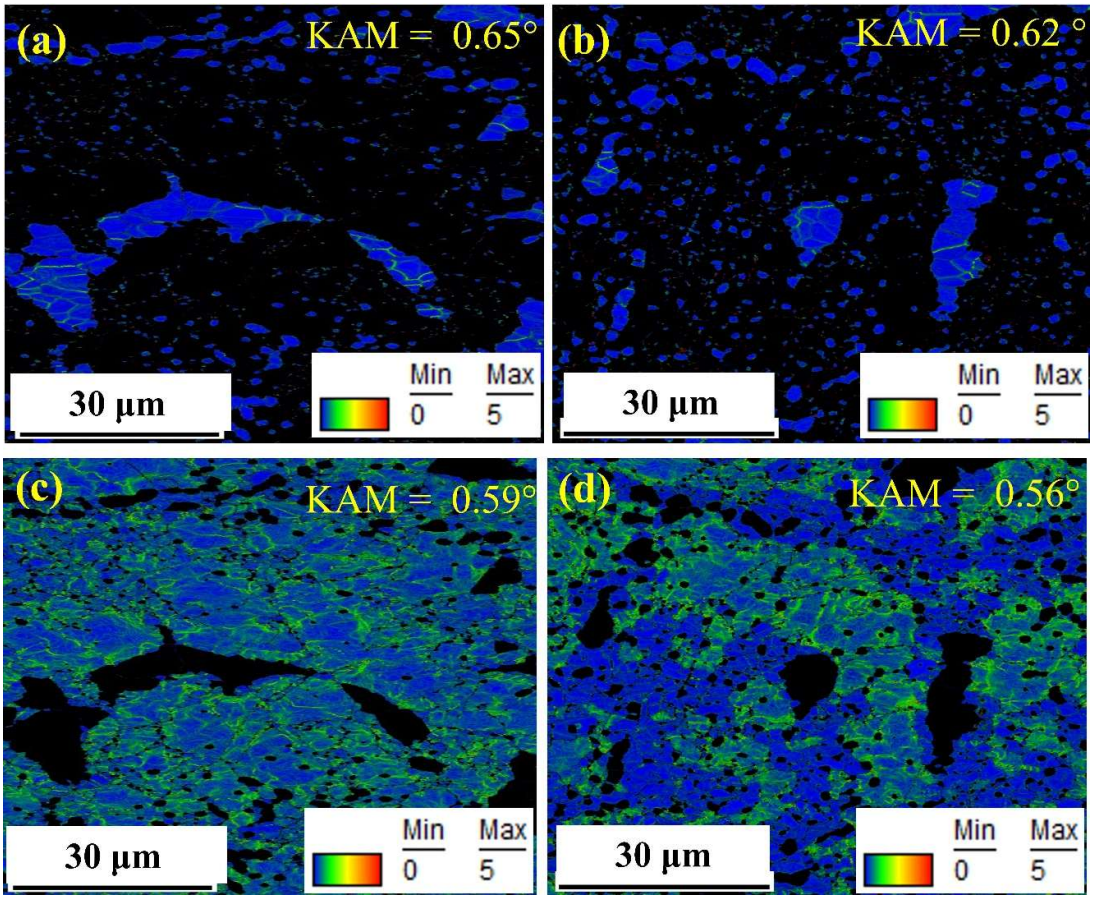

Figure 6.17: Kernel average misorientation maps of B2 in (a) PD3-AB_{30} with average KAM value of 0.65° and (b) PD3-AB_{30}E sample with average KAM value of 0.62°, austenite in (c) PD3-AB_{30} sample with average KAM value of 0.59° (d) in PD3-AB_{30}E with average KAM value of 0.56° suggesting the strain is reduced by electropulsing treatment.

Table 6.5:LAGB and HAGB fractions, average MA and KAM values of B2 and austenite.

Comparison	PD3-AB_{30}		PD3-AB_{30}E	
Phase	B2	Austenite	B2	Austenite
LAGB fraction	0.393	0.760	0.313	0.646
HAGB fraction	0.607	0.240	0.687	0.354
MA, (°)	26.2	13	29.7	19
KAM, (°)	0.65	0.62	0.35	0.56

The engineering stress-strain diagrams of the aged sample (PD3-AB_{30}) reports a yield strength of 1224 ± 11 MPa ultimate tensile strength (UTS) of 1430 ± 18 MPa, and plastic elongation of 10.3 ± 1.3 % (Figure 6.18) (Table 6.6). On electropulsing (PD3-AB_{30}E), YS reduces to 1197 ± 8 MPa, and UTS to 1398 ± 19 MPa, and the plastic elongation also increases to 17 ± 1 %. The product of strength and elongation increases from 14.7 GPa. % to 23.7 GPa. % after electropulsing treatment.

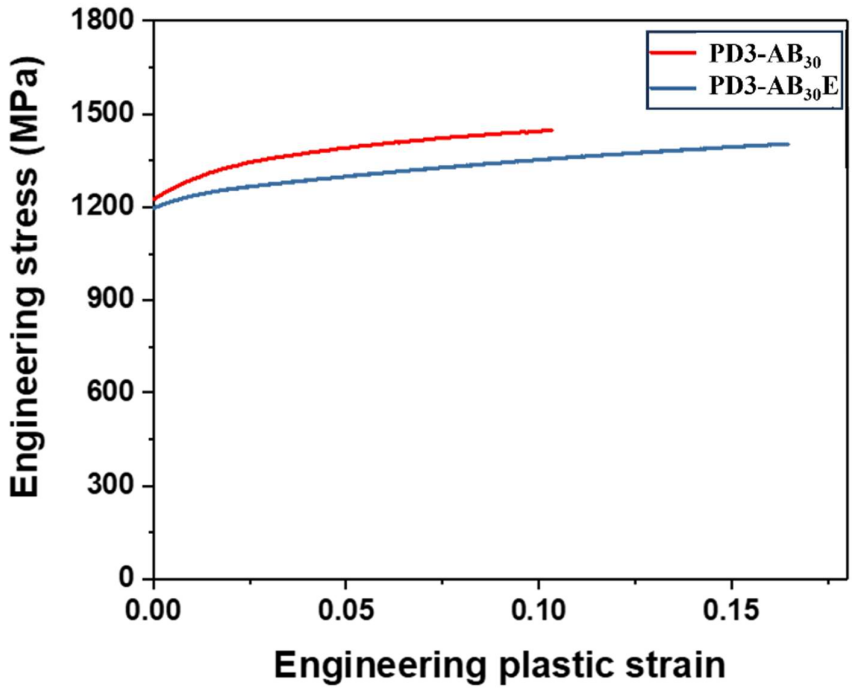

Figure 6.18: Engineering stress-plastic strain curves of PD3-AB_{30} and PD3-AB_{30}E low-density steels.

Table 6.6: Tensile properties of PD3-AB_{30}, PD3-AB_{30}E samples.

Sample	YS (MPa)	UTS (MPa)	El %	PSE GPa%
PD3-AB_{30}	1224 ± 11	1430 ± 18	10.3 ± 1.3	14.7
PD3-AB_{30}E	1197 ± 8	1398 ± 19	17 ± 1	23.7

6.3.2 Discussion

The observed microstructural modifications (dissolution, fragmentation, and spheroidization) induced by electropulsing can be attributed to two possible mechanisms: thermal effects and athermal effects. The thermal effects of electropulsing do not account for the observed changes in the microstructure as the theoretically calculated and experimentally measured temperatures (using an infrared thermometer), recorded as 291°C and 392°C, respectively. In contrast, the dissolution temperatures of B2 and k-carbide are considerably higher, surpassing 1200°C and 897°C, respectively. The electrical resistivities of the aged and electropulsed samples are determined to be $3.12*10^{-7}$ Ωm and $2.68*10^{-7}$ Ωm, respectively. The decrease in electrical resistivity is consistent with the thermodynamic predictions proposed by Dolinsky and Elperin whom proposed that a strong electric current causes a shift in the entire phase diagram curve due to the additional energy that inhibits the formation of nuclei with lower electrical conductivity [173]. Matthiessen's rule also states that when a material's impurity concentration is higher, its resistivity increases [153]. In the present case, k-carbides are enriched with Al and C, while B2 is enriched with Ni and Al compared to the matrix. Regarding morphology, k-carbides and B2 have lamellar and plate-like structures, resulting in higher resistance (R=ρ*l/A). As the electropulsing aims to increase conductivity, it either dissolves or fragments the phases that offer greater resistance. The driving force to overcome the barrier energy of dissolution is provided by momentum transfer between the moving electrons and dislocations (electron wind force). The change in free energy due to electric current ($\Delta G_{\epsilon lec}$) is expressed in equation 6.5.1 [174] as

$$\Delta G_{\epsilon lec} = \frac{\mu}{8\pi} \iint \frac{\vec{\iota_0}(r).\ \vec{\iota_0}(r\prime) - \vec{\iota_1}(r).\ \vec{\iota_1}(r\prime)}{|r-r'|}\ d^3r d^3r' \qquad [6.6.1]$$

Where μ is the magnetic permeability, r and r' are two positions within the material, $\overrightarrow{\iota_0}$, $\overrightarrow{\iota_1}$ are the current densities before and after electropulsing treatment.

Equation 6.5.1 is further modified as equation 6.5.2.

$$\Delta G_{\epsilon lec} = \mu g C i^2 \Delta v \qquad [6.6.2]$$

Where g is the geometric factor, C is the conductivity coefficient ($C = \frac{\sigma_2 - \sigma_1}{\sigma_1 + 2\sigma_2}$), Δv is the volume change, σ_1 and σ_2 are the electrical conductivities of B2/ k-carbide and austenite. As the conductivity of the matrix is more than the conductivities of precipitates, C < 0, thereby $\Delta G_{\epsilon lec}$ < 0. As a result, both B2 and k-carbide undergo dissolution. The deformation of B2/k-carbide is caused by the force exerted by the electron wind under high current densities. The reduction in YS and UTS by 27 and 32 MPa is due to the reduced fraction of k-carbide. A 6.7 % increase in total elongation is due to an increased fraction of HAGBs, dissolution, refinement, and fragmentation of precipitates. Thus, a significant improvement in tensile toughness is observed through EP of 61%. The increased fraction of HAGB is due to the coalescence of sub-grain boundaries in the electro pulsed sample [174]. These HAGBs act as more effective obstacles to plastic flow compared to low-angle grain boundaries (LAGBs) due to their large misorientation angle (>15°), wherein dislocations require a greater amount of energy to change the glide path from one grain to another.

6.3.2.1 Work hardening behavior

The variation in the work hardening rate concerning the true plastic strain curves for PD3-AB_{30} and PD3-AB_{30}E samples illustrates that there are only two stages i.e., stage I and stage II are found in both samples (Figure 6.19). The work hardening rates (θ_x) at the onset of stage I and stage II in PD3-AB_{30}, are 8913 MPa and 2561 MPa, respectively. For PD3-AB_{30}E, the respective work hardening rates are 5879 MPa and 2603 MPa. The transition strains (ε_x) corresponding to the end of stage I to stage II is 0.061 and fracture occurs at a

true strain of 0.1008, for PD3-AB_{30}. The transition strain for stage I in PD3-AB_{30}E is 0.0301 and for stage II, the transition strain increased up to 0.1541 till the fracture. A continuous decrease in the work hardening rate with increasing strain is observed in both samples. PD3-AB_{30} display substantially higher work hardening rates in comparison to that of respective stages in PD3-AB_{30}E and low transition strain at the end of stage II.

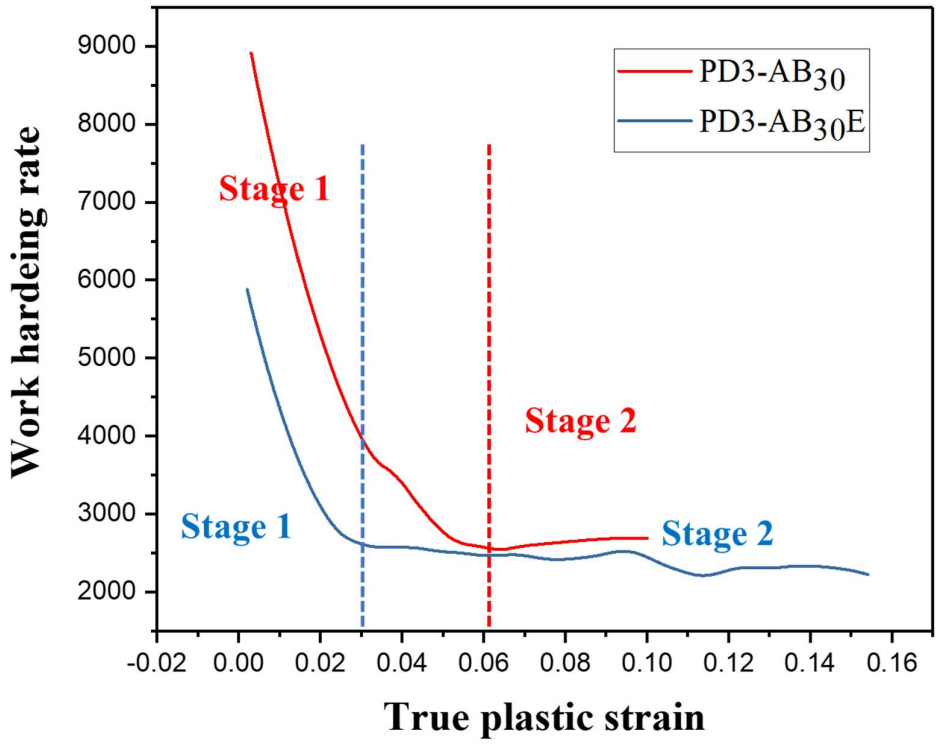

Figure 6.19: work hardening rate vs true plastic strain diagram for PD3-AB_{30} and PD3-AB_{30}E.

6.4 Comparison between tensile and work hardening behavior of annealed, aged samples and of their electropulsed ones

The engineering stress-strain curve of PD3-A reports a yield strength of 1015 ± 13 MPa ultimate tensile strength (UTS) of 1285 ± 17 MPa, and plastic elongation of 14.3 ± 2%. On electropulsing (PD3-AE), YS increases to 1077 ± 11 MPa, and UTS to 1355 ± 15 MPa, and plastic elongation to 19.6 ± 2%. The aged sample (PD3-AB_{30}) reports a YS of 1224 ± 11 MPa, UTS of 1430 ± 18 MPa, and plastic elongation of 10.3 ± 1.3 %. On electropulsing (PD3-AB_{30}E), YS reduces to 1197 ± 8 MPa, and UTS to 1398 ± 19 MPa, and the plastic elongation also increases to 17 ± 1 %. (Figure 6.20) (Table 6.7).

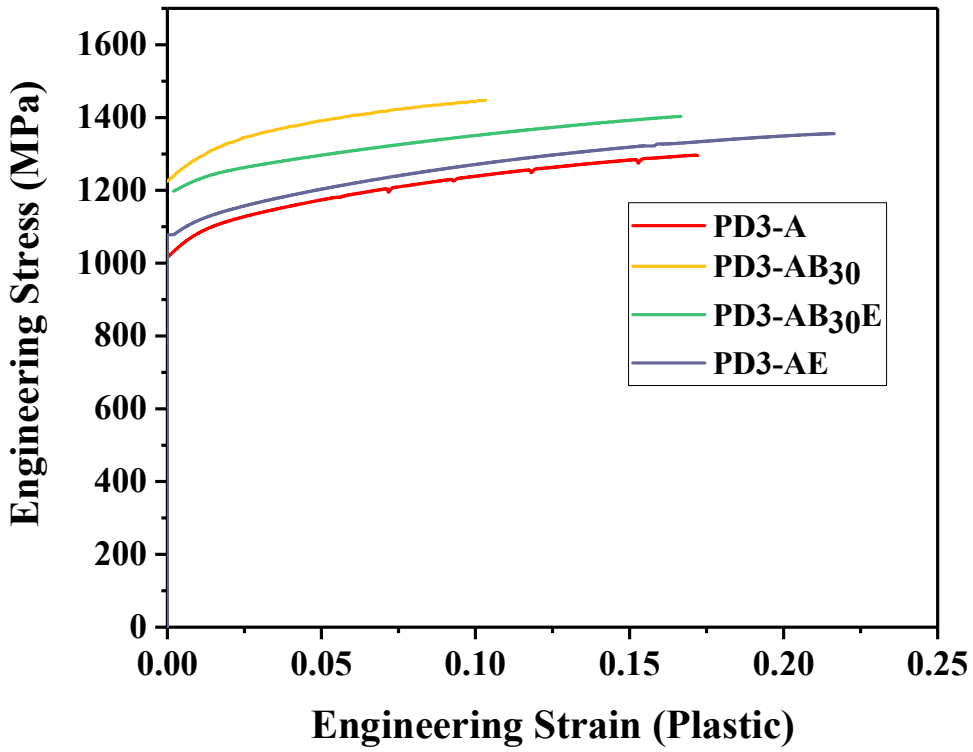

Figure 6.20: Engineering stress-plastic strain curves of PD3-A, PD3-AE, PD3-AB_{30} and PD3-AB_{30}E low-density steels.

Table 6.7: Tensile properties of PD3-A, PD3-AE, PD3-AB_{30} and PD3-AB_{30}E samples.

Sample	YS (MPa)	UTS (MPa)	El %	PSE GPa%
PD3-A	1015 ± 13	1285 ± 17	14.3 ± 2	18.3
PD3-AE	1077 ± 11	1355 ± 15	19.6 ± 2	26.5
PD3-AB_{30}	1224 ± 11	1430 ± 18	10.3 ± 1.3	14.7
PD3-AB_{30}E	1197 ± 8	1398 ± 19	17 ± 1	23.7

The variation in the work hardening rate concerning the true plastic strain curves for PD3-A, PD3-AE, PD3-AB_{30} and PD3-AB_{30}E samples illustrates that there are three stages (stage I-stage III) of work hardening observed in PD3-A and PD3-AE but only stage I and stage II are found in PD3-AB_{30} and PD3-AB_{30}E (Figure 6.21). Both electropulsed samples (PD3-AE, PD3-AB_{30}E) displays lower initial work hardening rates compared to their without electropulsed samples (PD3-A, PD3-AB_{30}).

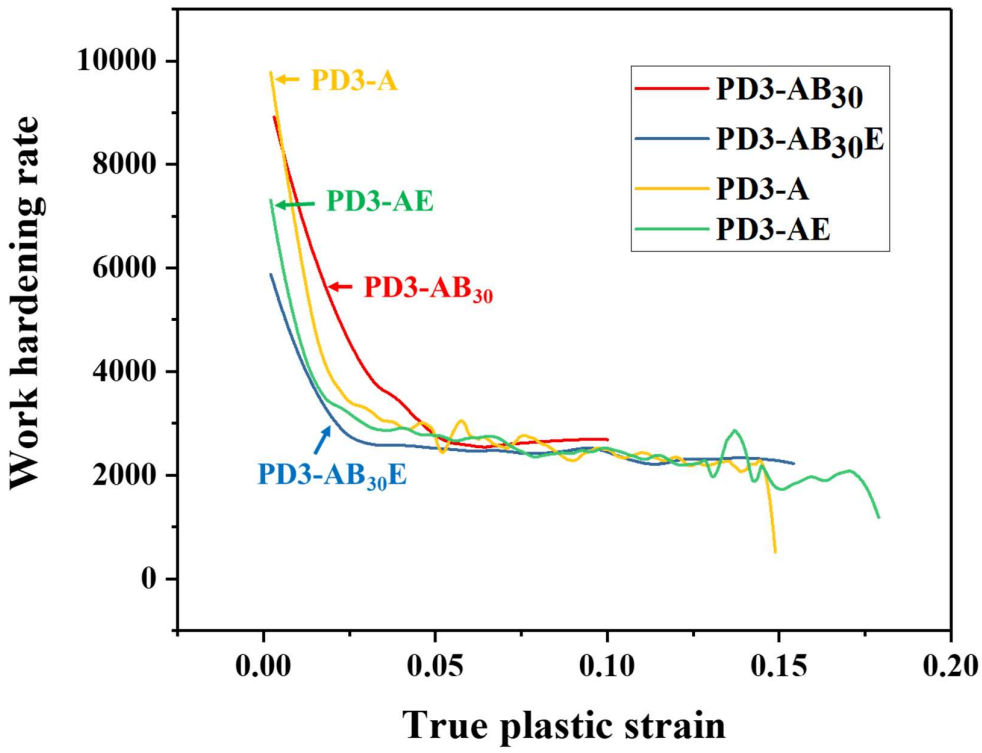

Figure 6.21: work hardening rate vs true plastic strain diagrams for PD3-A, PD3-AE, PD3-AB_{30} and PD3-AB_{30}E.

6.5 Conclusions

- Electropulsing of annealed duplex low-density steel, partially dissolves high temperature banded, globular and platelets of B2 precipitates at a low temperature of 346°C which is much below equilibrium solvus temperature (1242.2°C) due to reduction in activation barrier energy supplied mainly from the athermal electron wind energy. Localized dissolution results in the disintegration of platelets and reduction in the size of elongated bands as well as spheroids of B2.
- Shear stress exerted by the athermal electron wind force of electropulsing on dislocations is much higher than the critical resolved shear stress of B2. As a result, coarse precipitates are deformed as evidenced by elongated and fragmented bands

in the microstructure, and the development of new deformation texture component (221)[$1\bar{1}0$] of α fiber and decreased intensity of rotated cube component.

- The texture analysis of matrix austenite confirms that electropulsing dissolves the deformation texture components of Goss and S type but develops new ones of (012) <$0\bar{2}1$>, (021) <$0\bar{1}2$>, and (210) <$1\bar{2}0$> types.
- At a later part of electropulsing, when peak currents are low, the electric energy is insufficient for dissolution but the temperature goes down rapidly, the matrix is supersaturated and the precipitation is accelerated by the reduction in activation energy supplied from the electron wind of later part of the damped signal. Thus, a fine-sized additional B2 phase is precipitated.
- Dissolution and precipitation driven by electropulsing, refine the size of B2 and improves the distribution of size towards better uniformity. Electropulsing leads to spheroidization of existing precipitates by reduction in surface energy.
- The improvement in the yield strength (YS) and work hardening of selected duplex low-density steel by electropulsing is due to refinement by partial dissolution of B2 precipitate, improved size distribution as well as additional precipitation of fine globular form. Improvement in ductility and a higher amount of work hardening lead to higher ultimate tensile strength.
- The duplex low-density steel primarily follows Ludwigson flow behavior of initial rapid decrease in work hardening rate i.e. easy glide (Stage 1) followed by a steady-state (Stage 2) a balance between hardening by interaction and softening by cross-slip. At high strain, the material displays softening by dynamic recovery (Stage 3).
- The reduction in dislocation density, refinement in size of precipitate improvement in uniformity of its distribution, and partial recrystallization of austenite led to the increased plastic elongation from 16.3 to 21.6%. Even though both materials fail

by ductile-brittle mode, the increased size and area fraction of dimples further support additional plasticity in electropulsed low-density steel.

- Ageing of duplex low-density steel at 550°C precipitates kappa pearlite. Electropulsing of aged duplex steel breaks kappa carbides partially and spherodizes it due to reduction in barrier energy of dissolution and diffusion respectively.
- Refinement of B2, Dissolution of kappa carbide and spheroidization decrease YS and UTS but recovers tensile ductility and toughness.
- Work hardening rate of aged and electropulsed low density steel decreases similar to annealed steel but decreasing rate with strain is lower in aged and electropulse aged materials than that of annealed and electropulsing of annealed steel. The linear steady state work hardening rate of aged and electropulse aged steel in stage 2 is similar to annealed steel but ductility range is lower. There is no recovery softening stage in aged and electropulse aged steel.